NATIONAL AERONAUTICS AND SPACE ADMINISTRATION

Technical Report 32-1133

Surveyor Lunar Seismometer Instrument Development: Final Report

A. C. Dunk
E. O. Bulkley

JET PROPULSION LABORATORY
CALIFORNIA INSTITUTE OF TECHNOLOGY
PASADENA, CALIFORNIA

July 15, 1969

NATIONAL AERONAUTICS AND SPACE ADMINISTRATION

Technical Report 32-1133

Surveyor Lunar Seismometer Instrument Development: Final Report

A. C. Dunk
E. O. Bulkley

JET PROPULSION LABORATORY
CALIFORNIA INSTITUTE OF TECHNOLOGY
PASADENA, CALIFORNIA

July 15, 1969

Prepared Under Contract No. NAS 7-100
National Aeronautics and Space Administration

Preface

The work described in this report was performed by the Space Sciences Division of the Jet Propulsion Laboratory, under the cognizance of the *Surveyor* Project.

Acknowledgment

This report draws heavily from documented work of G. Sutton (principal investigator), R. Steinbacher (cognizant scientist), L. Van Hemelrijck, S. Thanos, A. T. Migliori, and C. B. Hord. Marshall Laboratories, Hamilton Watch Co., Hall-Sears, Inc., Geotech Division of Teledyne Industries, General Electric Co., and others have also contributed to the successful development of the *Surveyor* single-axis seismograph.

Lamont Geological Observatory (LGO), Columbia University, under contract to NASA, was given responsibility for the seismological aspects of the lunar experiments.

Contents

Tables

Figures

Contents (contd)

Figures (contd)

Contents (contd)

Figures (contd)

Abstract

This report presents a description of the single-axis seismometer developed for the lunar seismology experiment on the *Surveyor* Mission. The design, development, testing, and performance of the seismometer are discussed. Because of program changes, this experiment was not completed. However, the technology developed will be of direct benefit to the *Apollo* seismology experiment.

Surveyor Lunar Seismometer Instrument Development: Final Report

I. Introduction

The level of seismic activity occurring on a solid planet depends on the rate at which the stored elastic strain energy is dissipated by mechanical slippage. Temperature gradients which develop as thermal energy is generated by radioactive decay within the planet may cause internal stresses. However, if the planet is a good thermal conductor, seismicity from this cause is likely to be negligible. Actually, the rate of conversion of thermal energy into mechanical energy depends on the planet's thermal regime, which in turn is controlled by the concentration of radioactive elements, the initial temperature, and the rate of tidal energy dissipation. There is evidence which indicates that the moon is like earth: an active body with an interior that is probably hot.

The ultimate source of earthquake energy is believed to be some combination of the initial heat of formation of the earth and radiogenic heating. Theoretical studies of the thermal history of the moon indicate that an amount of energy equivalent to that released through earthquakes, about 10^{25} ergs per year, is available for moonquakes (Ref. 1). If this is true, one or more moonquakes per day sufficiently large to be recorded at any point on the moon and/or many more smaller events that could be recorded locally might be expected. It is possible that moonquakes will be concentrated in active zones (as are earthquakes), for example, along the margins of the maria. Meteorite impacts on the lunar surface might provide an additional source of seismic energy. Press et al. (Ref. 2) have estimated that the order of one impact per month could be detected with an instrument having a minimum detectable signal of 1 mμ. This estimate is, however, subject to a considerable amount of uncertainty. In the absence of moonquakes, meteorite or spacecraft impacts might provide the most efficient source of seismic energy for studying the interior of the moon. Provided that meteorite impacts can be differentiated from moonquakes, focal depth and other differences in source characteristics that may be deduced from the records can make the moon useful as a sounding board for the study of the distribution of meteorites.

Seismograph gravimeters sensitive to signals having periods as long as tidal periods (about 28 days) can provide information on the density and the elastic and anelastic properties of the interior of the moon from measurement of forced tidal deformations, free oscillations (having periods up to about 15 min) and long-period surface waves (Refs. 3–7).

A single short-period instrument, such as that developed for the *Surveyor* missions, can provide information from which the following may be deduced (because of difficulties in locating a natural event in time and space with a single recording instrument, a certain amount of ambiguity will be inherent in the data concerning many of these areas):

(1) Seismic activity: the number, magnitude, and spatial and temporal distribution of natural moonquakes.

(2) Elastic properties and structure: (a) near surface, obtained from body waves and short-period surface waves, and (b) at depth, obtained from body waves and intermediate-period surface waves.

(3) Distribution of meteorite impacts: the number and amount of energy released (dependent upon the ability to differentiate between impacts and moonquakes).

(4) Background noise level: the spectrum of seismic background noise correlated, if possible, with thermal, micrometeorite impact, and other sources, including those generated by the spacecraft.

From such information, inferences can be made concerning the existence of a low-strength "gardened" surface layer, a thick crustal layer, and a fluid core and their properties. The internal damping Q, density vs depth, temperature vs depth, and type and state of lunar material vs depth can also be inferred.

II. Seismograph Experiment Rationale

When *in situ* inspection of the moon became possible, the measurement of seismic activity on the lunar surface was one of the first geophysical experiments to be considered. Lamont Geological Observatory (LGO), under contract to NASA, was given responsibility for the seismological aspects of the lunar experiments.

Seismology experiments have been planned for all three NASA lunar landing programs: the unmanned *Ranger* (rough-landing) and *Surveyor* (soft-landing) programs, and the manned *Apollo* program. Short-period seismographs were flown on three unsuccessful *Ranger* missions (Ref. 8). These instruments were designed to withstand the extremely high decelerations associated with a rough landing. A four-component seismograph is being developed for use in the *Apollo* Lunar Surface Experiments Package (ALSEP), which will be set up on the lunar surface by the *Apollo* astronauts and left to operate for more than a year after their departure.

The prototype for the *Apollo* instrument was originally developed for the *Surveyor* Project (Refs. 8–10). However, because of weight and power restrictions, it was necessary to omit the long-period system from the *Surveyor* payload. The *Surveyor* short-period seismograph records the vertical motion component in a passband between 1/20 and 20 Hz.

By merely recording the degree of natural seismic activity (absent or present, high or low), much can be learned about the history and average composition of the moon. Much of the seismic background noise (microseisms) observed on earth is related to disturbances in the atmosphere and hydrosphere. These sources of noise are absent on the moon. However, some cultural noise related to the Surveyor spacecraft itself will be present. Resulting noise levels are expected to be low compared to those observed on earth. With the exception of discrete spacecraft events, which should be identifiable, the observed background should be the result of thermal stresses and a continuous shower of micrometeorites.

III. Instrument Design Considerations

The seismometer design is a compromise among the minimum detectable signal, the dynamic range and frequency response desired, simplicity and reliability, and the weight and power available. Equivalent input noise at the output of the seismometer amplifier is the sum of amplifier input noise and thermal noise generated in the resistive elements of the system input. With all other variables constant, the ratio of signal-to-noise power is directly proportional to the inertial mass of the seismometer sensor. The design goal of less than 1 mμ minimum detectable signal at 1 Hz was achieved using an inertial mass of 1.6 kg. The choice of a natural frequency of 1 Hz, nominal, for the mechanical suspension facilitates direct comparison with many existing short-period earthquake seismographs and permits reliable operation over the large temperature range expected even with the sensor tilted off the vertical by more than 15 deg (without resorting to auxiliary uprighting mechanisms). The instrument dynamic range of 46 dB is extended to 86 dB through three attenuation levels (0, -20, -40 dB) set by command.

Both the signal processing electronics and the seismic sensor are sensitive to temperature change. Adequate performance of the electronics was secured by selecting matching components whose performance tracked each other over the temperature range and by locating the electronics in a temperature-controlled compartment on

the spacecraft. The sensor is temperature-sensitive in three main areas: coil resistance, spring suspension, and magnetic field strength. The approach here, as with the electronics, is to design the sensor to be as insensitive to temperature as possible and to develop either passive or active temperature control as required to constrain the operating temperature to be within an acceptable range. The sensor will be rigidly attached to the spacecraft and may benefit from this. However, the thermal design of the sensor was developed assuming that the spacecraft would act neither as a sink nor a source of thermal energy and the sensor would be thermally insulated from the spacecraft.

The sensor, mounted rigidly on the *Surveyor* spacecraft rather than being deployed on the lunar surface, is coupled to the lunar surface through the transfer function of the spacecraft. This approach has the obvious advantage of simplicity and freedom from low-reliability deployment mechanisms plus having what was considered to be a more predictable thermal environment. Possible disadvantages from spacecraft resonances in the instrument band-pass and a higher noise level from vibrations produced by the spacecraft are balanced by the advantages of having the mechanical coupling to the lunar surface more predictable and more subject to analysis, using spacecraft data which may be obtained during landing. *In situ* calibration of the instrument will be accomplished by command through a pulse to the calibration coil which is equivalent to a step in the sensor case acceleration.

It is expected that, within the constraints imposed by spacecraft and communications capabilities and the operation of other instruments, the seismograph will be operated for the maximum time possible following *Surveyor* landing. Mechanically noisy spacecraft operations will not damage the instrument but may make the affected portions of the data unusable.

Seismic data will be telemetered to earth and recorded on standard seismograph drum recorders (using various filter settings) and on magnetic tape. Data can be conveniently digitized directly from the magnetic tape for subsequent automatic digital or analog processing.

IV. Seismograph System Design

A. General Concepts

In normal earthbound seismology, knowledge of the anticipated motion and the intended use of the seismograph dictates instrument selection and the adjustments which are to be made. For instance, instrumental sensitivity may be set to record the extremely small motions generated by small or distant earthquakes. Conversely, the type of seismograph may be selected to measure strong local shocks, which are capable of damaging intensity at close range. In general, a single instrumentation system has insufficient dynamic range to accommodate both applications. The expected frequency spectrum must be considered; for terrestrial seismology, the microseismic spectrum, with its high peak in the region of 6-s period, neatly divides seismographic instrumentation into two broad regions: short-period (frequencies above approximately ½ Hz) and long-period (frequencies below the ⅙-Hz microseismic noise peak).

As is the case in communications and electronics in general, the gain-bandwidth product is a measure of the difficulty of a recording task or of the merit of an amplifier. The same is true of seismographic systems; hence to broaden the bandwidth capability while maintaining maximum sensitivity to small signals and good margin from overload due to large signals is a difficult task.

In the case of lunar seismology, an estimate of anticipated lunar motion must be made in order to establish the seismographic system parameters, but the absence of prior knowledge complicates the task of estimation. Provision for variable amplifier gain, adjustable on command, helps to minimize the penalty for an originally inaccurate estimate. Severe constraints are imposed on a lunar seismology experiment by (1) maximum weight and power requirements imposed by the spacecraft limitations and (2) the requirements (as far as *Surveyor* is concerned) that the instrument be positioned and operated without local manual assistance.

In the design of any seismographic system in which the sensor is followed by an electronic amplifier, the overall system sensitivity is a function of both the inertial mass within the sensor and the gain of the amplifier; the limitation to maximum system sensitivity is imposed by amplifier input noise.

For the lunar application, a satisfactory compromise was reached which specifies a short-period vertical component sensor with lunar natural period of nominally 1.3 s, inertial mass of approximately 1.68 kg, and maximum amplifier gain of 100 dB.

More complete descriptions of the system parameters actually achieved are presented in a following section.

B. Electronics Design

The following discussion is based upon the electronic design which was developed at the inception of the *Surveyor* seismometer program, originally published in Ref. 11. At the inception of the *Surveyor* Project, the science of electronic circuit design was not as comprehensive as it is now, and design decisions made today would vary from those originally adopted. This section should be read, therefore, with this in mind.

Basically, the short-period seismometer consists of a coil mounted within the flux gap of a suspended permanent magnet which serves as the inertial mass. Motion of the suspended magnet relative to the main coil induces a voltage proportional to the differential velocity. A very-high-gain low-noise amplifier is required to amplify the minute level of seismometer output power to the levels required by telemetry. The requirements originally imposed on this amplifier were:

(1) Equivalent input noise less than 1 μV peak-to-peak for 90% of the time, with a source impedance of 800 Ω.

(2) Minimum possible power consumption.

(3) Bandwidth within 3 dB from 0.05 to 20 Hz.

(4) Input impedance equal to the value required for damping the seismometer (0.7 critical damping).

(5) Output impedance less than 500 Ω.

(6) Output swing capability of 0–5 V into 50-kΩ load.

(7) Satisfactory performance over a temperature range of -20 to $+180$°F.

The response of a properly damped seismometer is essentially flat to ground displacement for frequencies above its natural frequency and to ground acceleration below its natural frequency. Since the velocity transducer differentiates this motion, its output is flat to ground velocity above the natural frequency. If the amplifier response is flat over the specified range, then the overall system response is that of the sensor itself in the above frequency range.

With a 5-V maximum output signal and an anticipated telemetry dynamic range of 46 dB, the minimum detectable output is 25 mV. The transducer output across its damping resistance is of the order of 0.6 μV pp per mμ (10^{-9} m) pp ground displacement at 1 Hz. If an amplifier with an equivalent input noise of the order of ½ μV could be designed, it would be possible to detect the above ground displacement with an overall amplifier voltage gain of 44,000. If lower noise voltages could be achieved, the gain could be increased accordingly. Without any knowledge of background seismic noise (microseisms) on the moon, it is impossible to decide exactly what gain to use in the amplifier. In general, the moon is thought to be much quieter than the earth, and maximum possible gain may be appropriate. If, however, this is not the case, a high-gain amplifier could saturate on background alone. Two solutions to this problem exist: a nonlinear amplifier and an amplifier with gain adjustable on command. The second solution was chosen in this case and a step attenuator incorporated in the amplifier.

In view of the extremely low frequencies involved, the chopper-amplifier was probably the best choice for seismic work at that time. Very low noise levels may be achieved with good mechanical or photoelectric choppers. These, however, had to be ruled out in this case because of power limitations and environmental requirements. Solid-state choppers on the other hand did not offer much promise in achieving the desired noise levels.

A compromise was reached with a design that employs a solid-state chopper-amplifier preceded by a direct-coupled low-noise preamplifier with a single low-frequency coupling between the two. Thus dc drift from the preamplifier is not amplified further by the carrier amplifier. The complete circuit block diagram is shown in Fig. 1. In order to utilize the advantages of a balanced arrangement in the preamplifier, the seismometer main coil was center-tapped, thus providing a push-pull output. The output of the preamplifier is filtered and applied to the modulator followed by another stage of push-pull amplification. The modulated signal is then applied, through the attenuator, to the following stages of ac amplification. It is then demodulated and filtered.

C. LGO Electronics: Detailed Description

1. Preamplifier. The preamplifier consists of two direct-coupled differential stages with overall direct feedback. The feedback stabilizes the operating point, the current gain, and the input impedance presented to each half of the center-tapped transducer coil. The amount of feedback is chosen to adjust the amplifier input impedance to that required for damping the seismometer without use of an external damping resistor. Thus the maximum power level is transferred to the input of the amplifier.

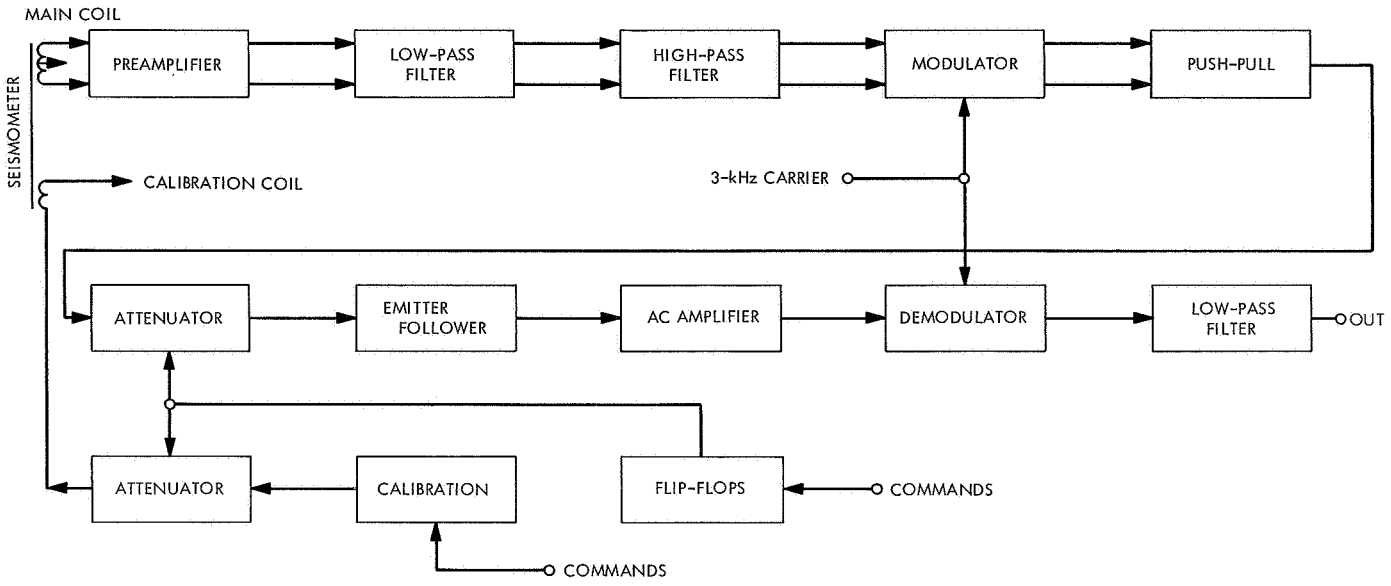

Fig. 1. Block diagram of short-period lunar seismograph

Several transistor types were tested in a preliminary circuit configuration. Very encouraging results were obtained from two matched pairs of 2N930's (a high-β, low-noise-type of planar construction[1]). Current construction utilizes a 2N2642 as replacement for each pair of 2N930's. On the basis of the noise test, it was decided that an overall gain of the order of 250,000 should be realizable. A preamplifier gain of the order to 500 was decided upon. The first-stage transistor collectors are biased at approximately 5 V and 100 μA. By returning the emitters to a negative supply through a large resistor (Fig. 2), the center-tap of the seismometer coil can be grounded and a good common-mode rejection achieved. Diode clippers are shunted across each input to protect against accidental excessive input signals.

Without any feedback, the input impedance of each side would be much higher than required (between 0.5 and 1 kΩ).

By employing shunt feedback from the output collectors to the input bases (Fig. 3), the current gain is reduced by

$$A_i = \frac{A_{io}}{1 + \frac{Z_L}{Z_{fb}} A_{io}} \cong \frac{Z_{fb}}{Z_L}$$

For large values of open-loop current gain, the input impedance, which is essentially unaffected by the overall feedback, is then

$$Z_i = \frac{A_i}{A_v} Z_L \cong \frac{Z_{fb}}{Z_L} \frac{Z_L}{A_v} \cong \frac{Z_{fb}}{A_v}$$

where A_v is the voltage gain (Ref. 12).

Thus, to obtain a stable input impedance, the voltage gain must be stabilized. This is done through local emitter degeneration in both stages.

For a preamplifier voltage gain of 500 and a nominal input impedance of 850 Ω, we compute the feedback resistance as

$$Z_{fb} = A_v Z_i = 500 \times 850 = 425\,\text{k}\Omega$$

From bias considerations, neglecting loading by the following stage on the preamplifier output, the second-stage collector load is of the order of 20 kΩ. Thus, the closed-loop current gain will be approximately

$$A_i = \frac{Z_{fb}}{Z_L} = \frac{425}{20} = 21$$

A complete analysis of the gain of the circuit shows that for the worst combination of parameters the voltage gain may vary from 430 to 980 about a design center of 600. Thus despite the fact that the input impedance is largely determined by feedback rather than transistor parameters, the spread is considerable, ranging from

[1]Bulletin DL-S611873, Texas Instruments Inc., Dallas, Tex., August 1961.

approximately +40 to −38%, about a design center of 840 ohms. The corresponding spread in damping factor, however, is considerably less, since damping is inversely proportional to the sum of transducer impedance plus amplifier input impedance. The damping factor ranges from +21 to −15.6% about the design center.

If the above variation is objectionable, either the input transistors must be selected or the input impedance experimentally adjusted to provide the correct damping at room temperature. This may be done conveniently by selecting the value of the feedback resistance. The calculated variation in damping factor in this case is shown in Table 1 for different combinations of transistor parameters. It is seen that control within 10% may be obtained. An alternate method of improvement would be to reduce the preamplifier gain while increasing the gain of the postamplifier. The disadvantage of this approach lies in the fact that the output temperature drift resulting from carrier voltage leakage in the modulator will increase.

Table 1. Damping factor variations for combinations of transistor parameters

Combination of parameters	Variation in damping factor, %			Required Z_{fb} kΩ
	Lowest temperature	Room temperature	Highest temperature	
Design center	7.0	0	−6.2	510
Min-min	1.9	0	−4.7	510
Max-max	9.5	0	−10.2	500
Min-max	8.9	0	−8.5	670
Max-min	4.0	0	−5.6	410

$$\%\Delta D = \frac{Z_{i0} - Z_i}{Z_G + Z_i} \times 100$$

where

$Z_{i0} = 840\ \Omega$ and $Z_G = 1000\ \Omega$.

It is now appropriate to examine how the above variations in internal preamplifier gain and input impedance affect the overall transducer gain. Let the overall transducer gain be denoted by A_t where

$$A_t = \frac{\textit{Preamplifier output voltage}}{\textit{voltage induced in seismometer coil}}$$

The expression for A_t in terms of A_v, Z_i, and source impedance Z_G is:

$$A_t = \frac{Z_i}{Z_G + Z_i} A_v = \frac{Z_{fb} A_v}{Z_{fb} + Z_G A_v}$$

Differentiating the above, we obtain

$$dA_t = \frac{(Z_{fb})^2}{(Z_{fb} + Z_G A_v)^2}\, dA_v$$

and since

$$\frac{(Z_{fb})^2}{(Z_{fb} + Z_G A_v)^2} < 1$$

the variation in A_t is always smaller than the variation in A_v. In particular, for $Z_{fb} = 500$ kΩ, $Z_G = 1$ kΩ, $A_v = 600$, we find that

$$dA_t \cong 0.2\, dA_v$$

Thus, the overall gain tends to be nearly constant, independent of transistor parameter variation.

2. Modulator. The balanced output from the preamplifier is coupled through an appropriate filter to a half-wave bridge modulator.

3. AC amplifier. This amplifier consists of two direct-coupled stages feeding the transformer-coupled demodulator. The operating points and gain are stabilized through separate dc and ac feedback loops. The requirements imposed on this amplifier are:

Gain: 100 maximum, with convenient means of adjusting it to lower values (if necessary).

Gain stability: 10%.

Phase shift: 0 deg at 3 kHz.

Output swing: at least 10 V pp.

Output impedance: less than 500 Ω.

Input impedance: no stringent requirement (driven by an emitter follower).

The operating point of the second stage is chosen to provide the maximum swing into the output load, which is effectively the feedback resistor, since the demodulator input impedance is very high. The operating point of the first stage is determined by the emitter voltage of the second stage, since direct coupling is employed. The base bias for the first stage is derived from a tap in the emitter resistance of the second stage. This arrangement together with the large emitter resistance of the first stage results in an extremely stable amplifier.

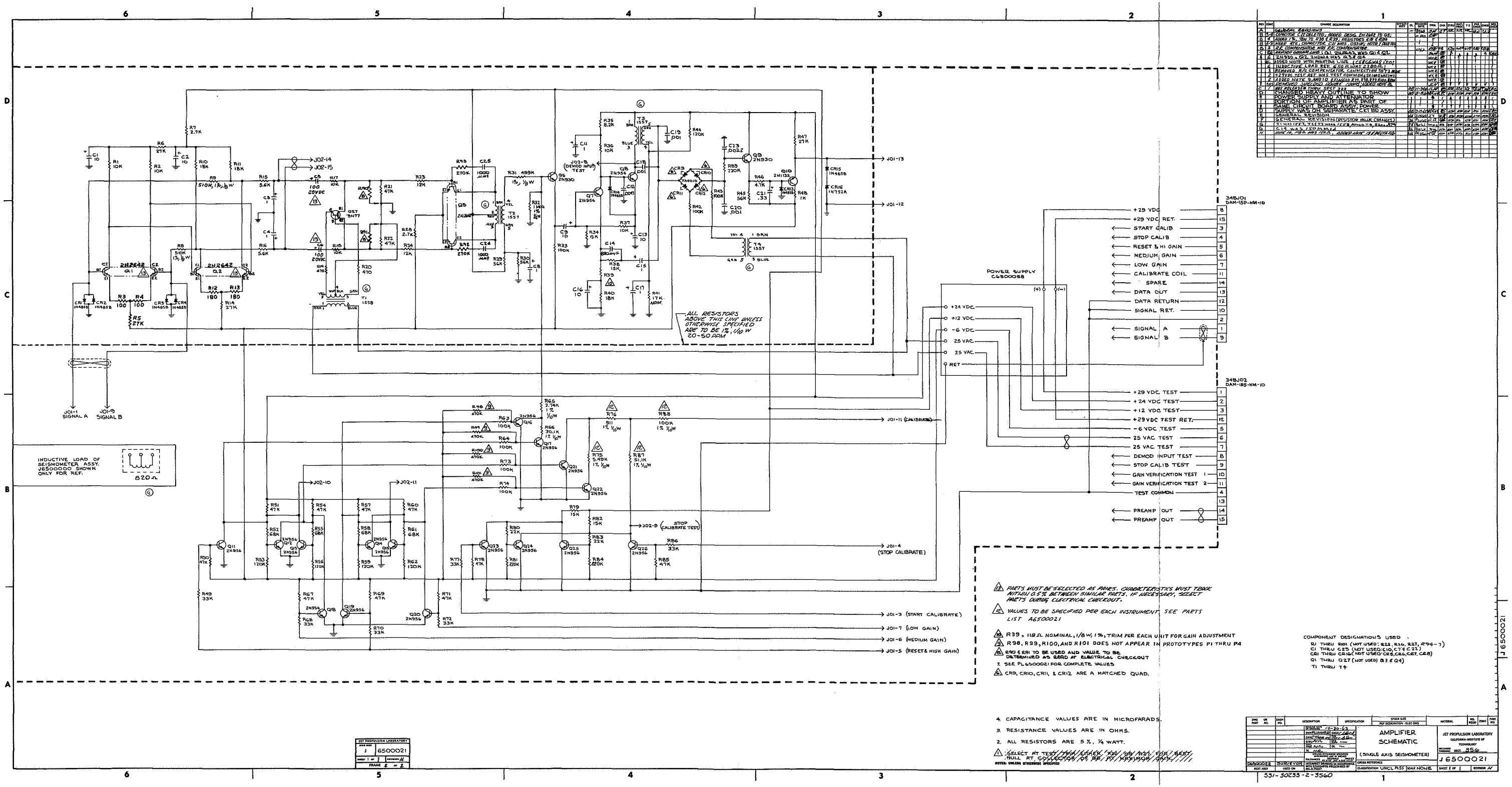

Fig. 2. Amplifier schematic diagram

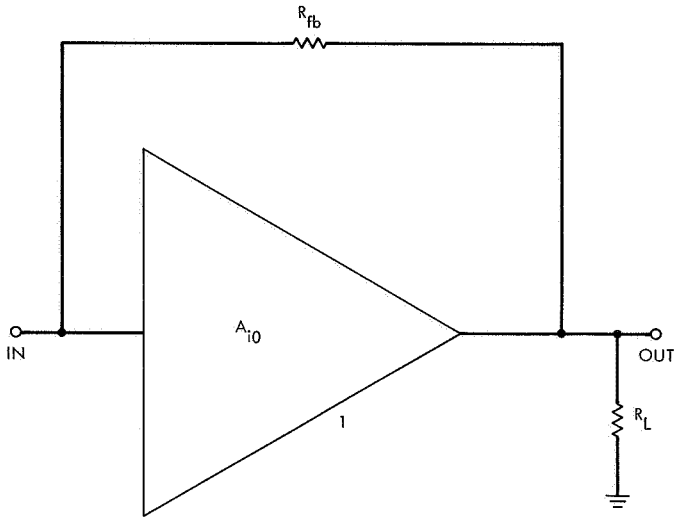

Fig. 3. Amplifier with shunt feedback

A complete analysis of the ac gain of the circuit shows that, for the worst combination of transistor parameters, the open-loop gain may vary from 850 to 5800 over the temperature range of -20 to $+100°C$. If the feedback factor is $B = 0.01$, then the corresponding variation in closed-loop gain is 89.5 to 98.2, with a design center value of 96. Thus the gain may be specified as

$$A = 96 \begin{smallmatrix} +2.3 \\ -6.8 \end{smallmatrix} \%$$

and the stability requirement has been met.

The gain of the amplifier may be reduced by increasing the feedback while decreasing the open-loop gain without affecting the stability.

4. Demodulator. The demodulator is a half-wave diode bridge arrangement. The output is fed to an emitter-follower that provides a high impedance to avoid loading of the demodulator.

A single-stage low-pass RC filter is inserted at this point to suppress high-frequency components of the demodulated signal.

5. Step attenuator. It is desirable to maintain the calibration output pulse at a constant percentage of full-scale reading independent of the gain setting. This can be done by inserting an attenuator, which varies inversely as the gain setting, between the calibrate pulse generator and the seismometer calibration coil.

A circuit was designed which performs this function upon reception of the appropriate command trigger. As shown in block diagram form (Fig. 4), the circuit consists of two flipflops driving four transistor switches. Attenuator I is the amplifier gain attenuator and attenuator II is the attenuator of the calibrating voltage. A total of three steps of gain change can be obtained as follows:

Trigger 1 resets FF_A and FF_B to the states shown. Thus, S_1 and S_2 are open and S_3 and S_4 are closed. This is the position of maximum amplifier gain and minimum calibrating voltage output. Trigger 2 reverses the state of FF_A only, thereby closing S_2 and opening S_3. This is the position of intermediate gain and calibrating voltage. Finally, trigger 3 reverses the state of FF_B only, thereby closing S_1 and opening S_4. This is the position of minimum gain and maximum calibrating voltage. The sequence is not reversible in that if it is desired to change from minimum to intermediate gain, one must go through maximum (reset) gain first. The attenuation factors attainable are only limited by the on and off resistances of the transistor switches. A very large attenuation would necessitate a very small value of R_2 and is eventually limited by the saturation resistance of transistor S_1. Germanium transistors would, in this case, offer an improvement owing to lower saturation resistance.

The input ac signal must be polarized for proper functioning of the switches.

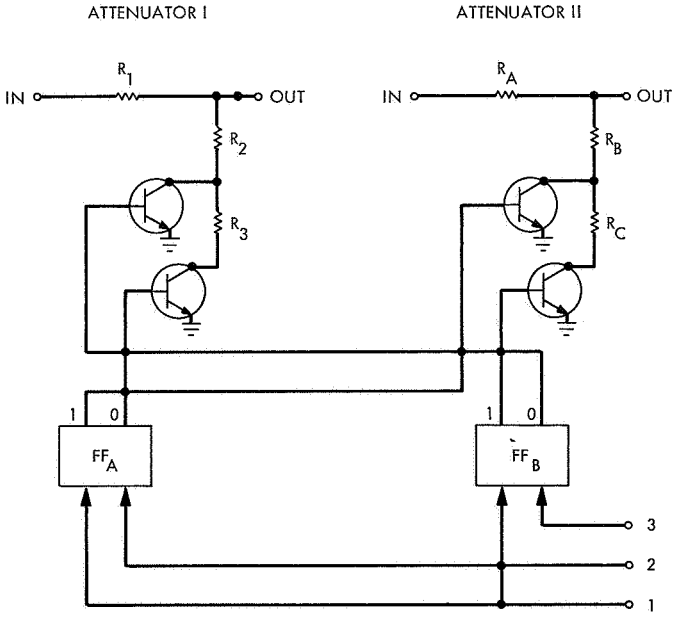

Fig. 4. Block diagram of command-controlled step attenuator

Direct-coupled transistor triggering of the flipflops makes performance independent of trigger characteristics. The attenuator flipflops are "worst case" designs and will function properly throughout the temperature range.

6. Calibrator. The calibrator is simply a flipflop which, when triggered by a command pulse, produces a current step in the auxiliary coil of the instrument. The step is subsequently turned off by another command pulse after a satisfactory transient at the output is obtained. The advantages of such an arrangement over a free-running pulse generator are obvious and need not be discussed further.

As discussed previously, the size of the step is inversely proportional to the gain. Thus, the output pulse amplitude is independent of gain setting. The peak amplitude of the output transient is approximately 25% of full scale.

To compensate for instability due to high-frequency phase shift in the output transformer of the carrier amplifier, corrective networks were incorporated in the feedback loop. The values of the components were determined experimentally to provide ample phase and gain margins. The open-loop transfer function and frequency response of this amplifier are shown in Figs. 5, 6, and 7. The output swing capability is approximately 15 V pp, and the output impedance is very low owing to the heavy ac feedback. Temperature test results are shown in Fig. 8.

The performance of the attenuator, adjusted to give 20-dB steps, is shown in Fig. 9. For any particular setting, the performance is substantially linear over the required dynamic range.

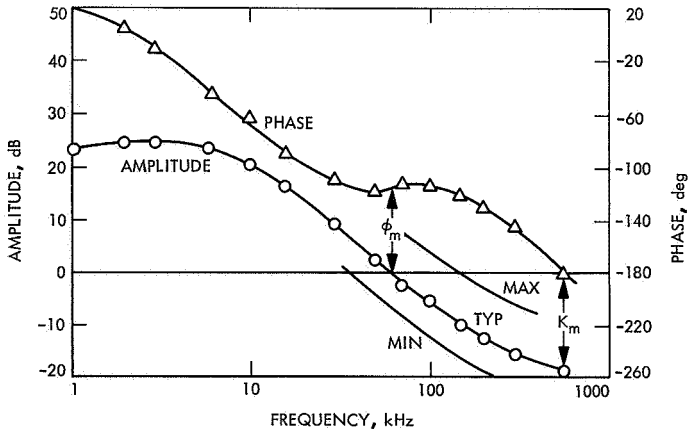

Fig. 5. Transfer function of ac amplifier (high end)
Typical gain margin K_m = −18 dB and phase margin = +65 deg.

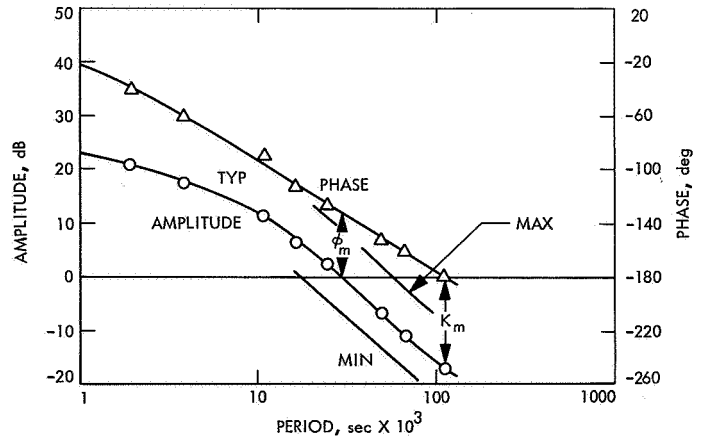

Fig. 6. Transfer function of ac amplifier (low end)

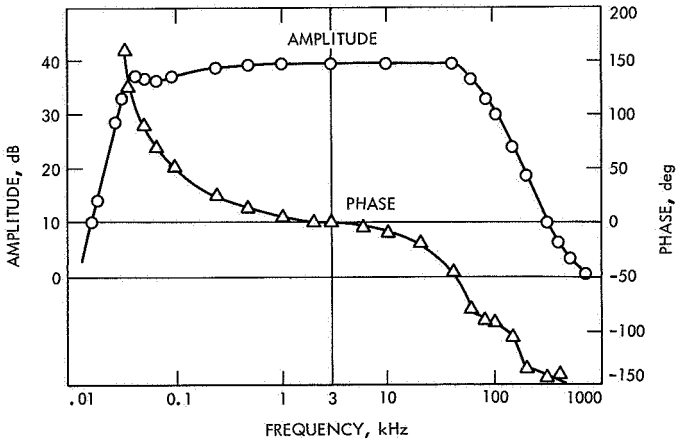

Fig. 7. Frequency and phase response of ac amplifier showing zero phase shift at the carrier frequency of 3 kHz

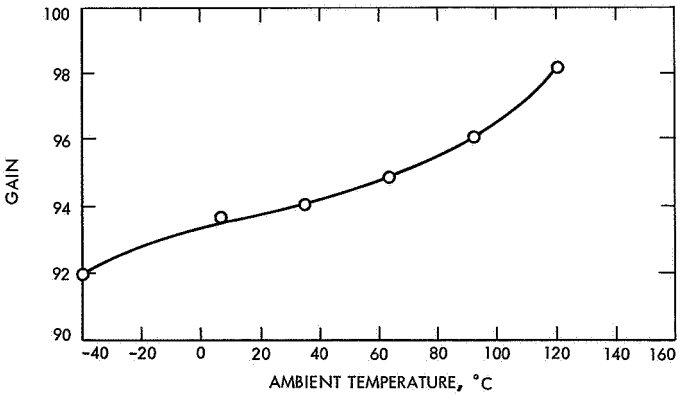

Fig. 8. Variation of ac amplifier gain with temperature

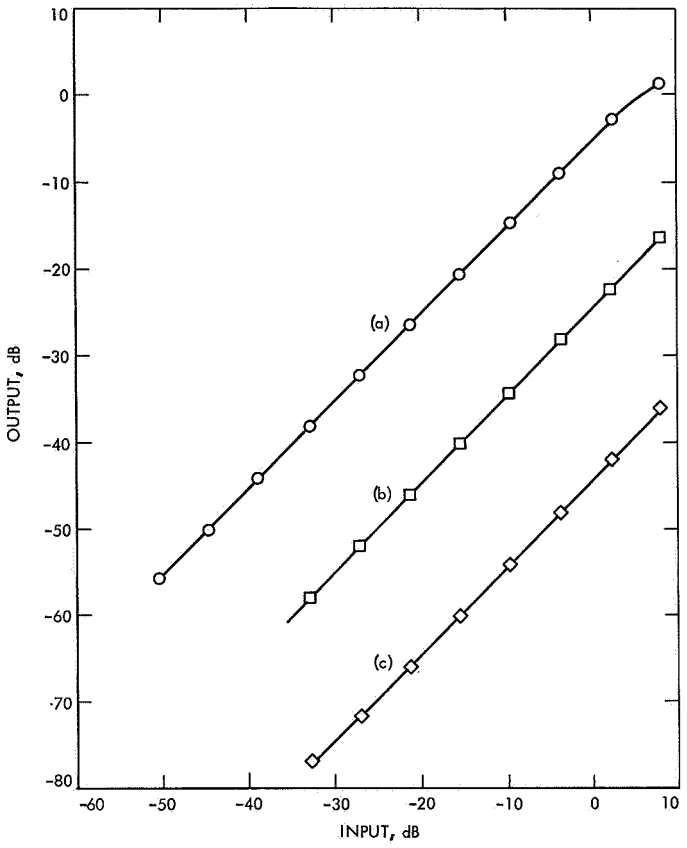

Fig. 9. Attenuator characteristics for steps of 20 dB
(a) 0-dB attenuation, (b) 20-dB attenuation, (c) 40-dB attenuation. The insertion loss of the attenuator is 6 dB.

Representative waveforms at various points of the complete amplifier circuit are shown in Fig. 10. These are self-explanatory. The entire amplifier was subjected to a temperature test at maximum gain. The output drift shown in Fig. 11 is the combined result of carrier leakage in the modulator, temperature drifts in the demodulator, and the small variation in carrier amplifier gain. The frequency response of the amplifier is plotted in Fig. 12. The 3-dB frequencies are 0.035 and 22 Hz. Thus the minimum bandwidth requirement has been achieved.

Figure 13 shows the output noise achieved with an overall gain setting of 0.5×10^6, recorded at several chart speeds. It is seen that for 90% of the time the output noise does not exceed 100 mV, which corresponds to an equivalent input noise of 0.2 μV pp.

A noise figure measurement is not very meaningful in seismic work. A better estimate of the capabilities of the amplifier can be obtained by examining the output waveforms (see Figs. 14 and 15). These correspond to respective inputs of 1 and ¼ μV pp, obtained with the same recorder sensitivity and speeds as in Fig. 13.

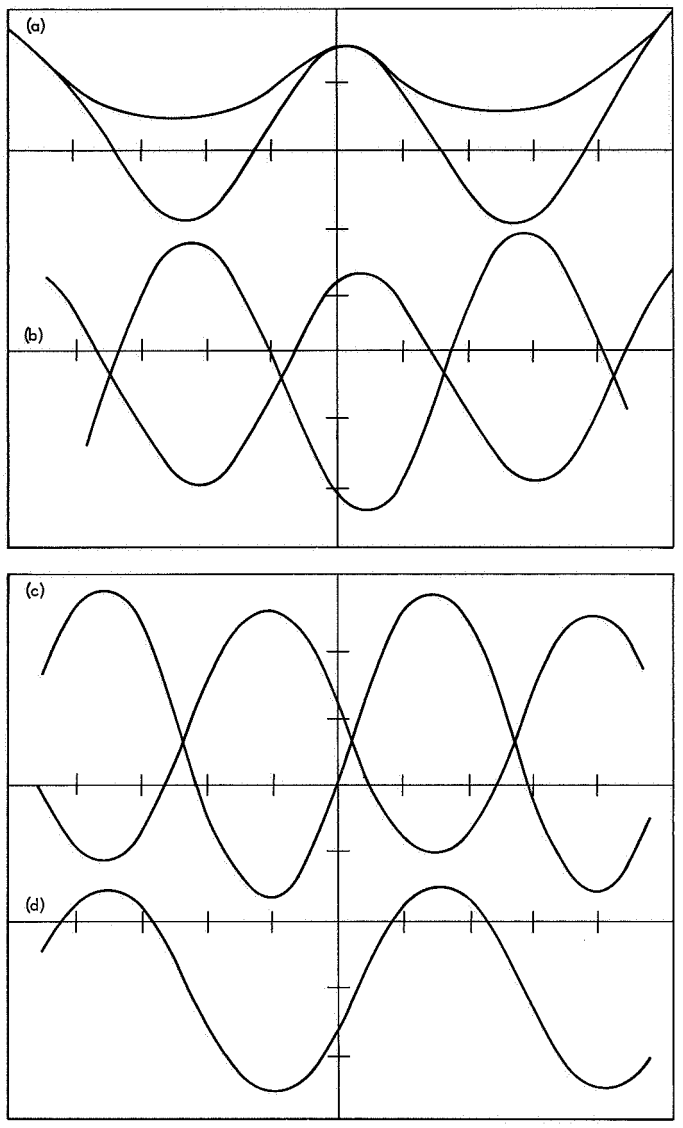

Fig. 10. Amplifier waveforms obtained by driving the calibration coil of the seismometer from a 0.5-Hz current source at minimum gain (from Ref. 11)
(a) modulator output (either side to ground), 0.1 V/cm; (b) attenuator input, 2 V/cm; (c) demodulator input, 1 V/cm; (d) seismic output, 1 V/cm.

In particular, a 1-Hz input of ¼ μV is detected with a S/N ratio of about 4:1. For the aforementioned transducer sensitivity of 0.6 μV/mμ pp at 1 Hz, it appears possible to detect 1 Å pp ground motion at 1 Hz with unity S/N ratio.

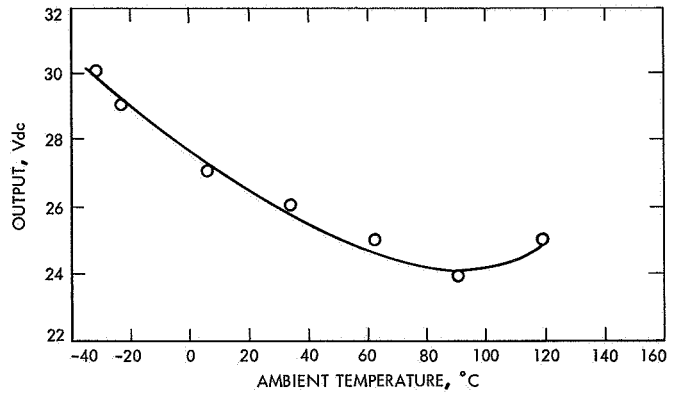

Fig. 11. Variation of amplifier output dc level with temperature

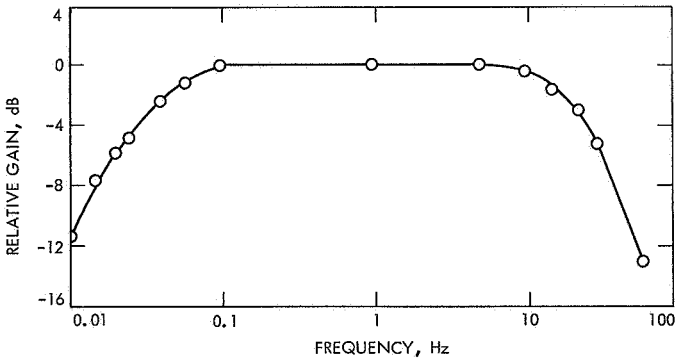

Fig. 12. Frequency response of amplifier
The 3-dB frequencies are 0.035 and 22 Hz.

The program schedule dictated the need to terminate the development effort and proceed with the manufacturing phase. Accordingly, the electronic amplifier design was frozen in a state essentially as described in the preceding pages. Manufacture was completed by Marshall Laboratories, under JPL contract 951396. Problems which arose during the manufacturing phase were disposed of by joint efforts of A. T. Migliori, cognizant JPL engineer, and Marshall Laboratories personnel. A minimum of redesign and circuit modifications was actually required.

D. Electronics Study Program

1. General. Inevitably, the state of the electronics art advanced, particularly with respect to solid-state devices and field-effect transistors. It was obvious that more advanced techniques could improve performance of the seismic amplifier, and a parallel (but essentially independent) analysis and study program was being pursued during manufacture of the originally designed electronics. A description of this effort is the subject of a memo dated

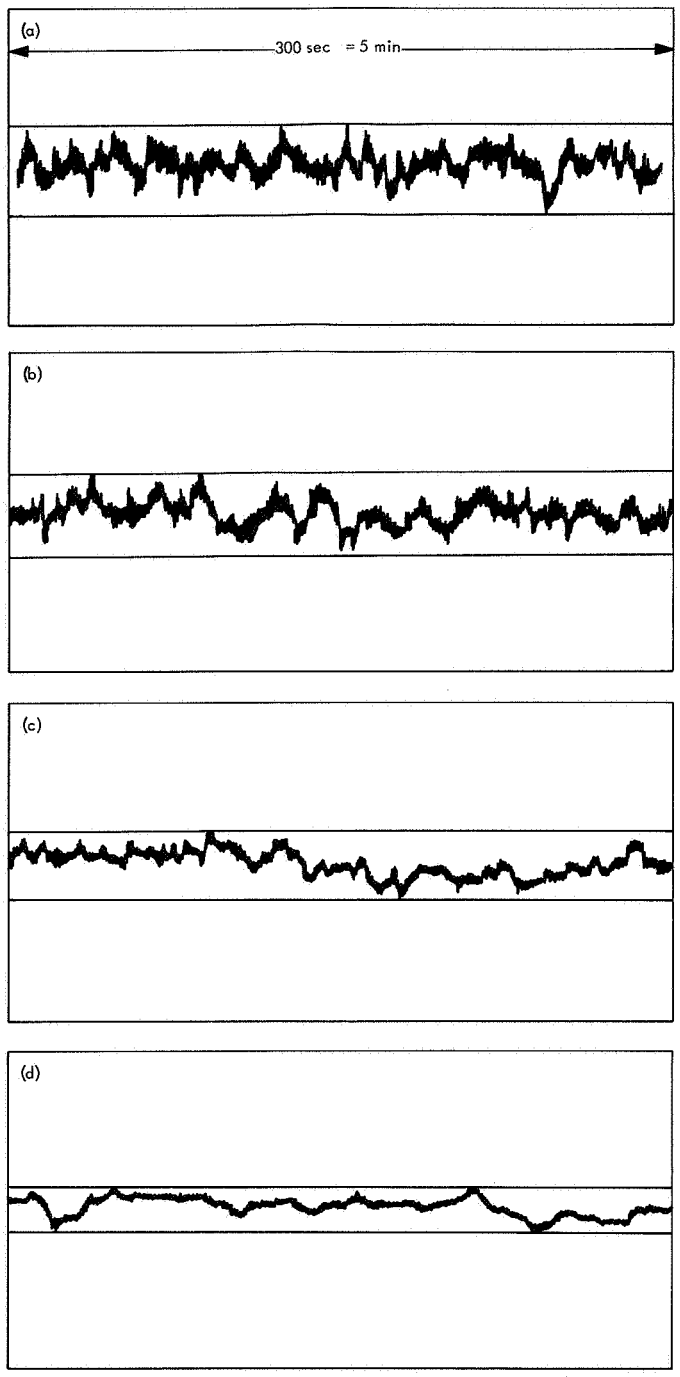

Fig. 13. Output noise of the amplifier with an overall gain of ½ million
Recorder sensitivity is 200 mV/cm and speed is (a) 0.5 mm/s, (b) 1 mm/s, (c) 10 mm/s, (d) 100 mm/s.

July 1966, by R. A. Schindler of JPL. The essence of this memo is presented below in condensed form.

Of particular interest is the automated approach to noise measurement, which contributes much in the way

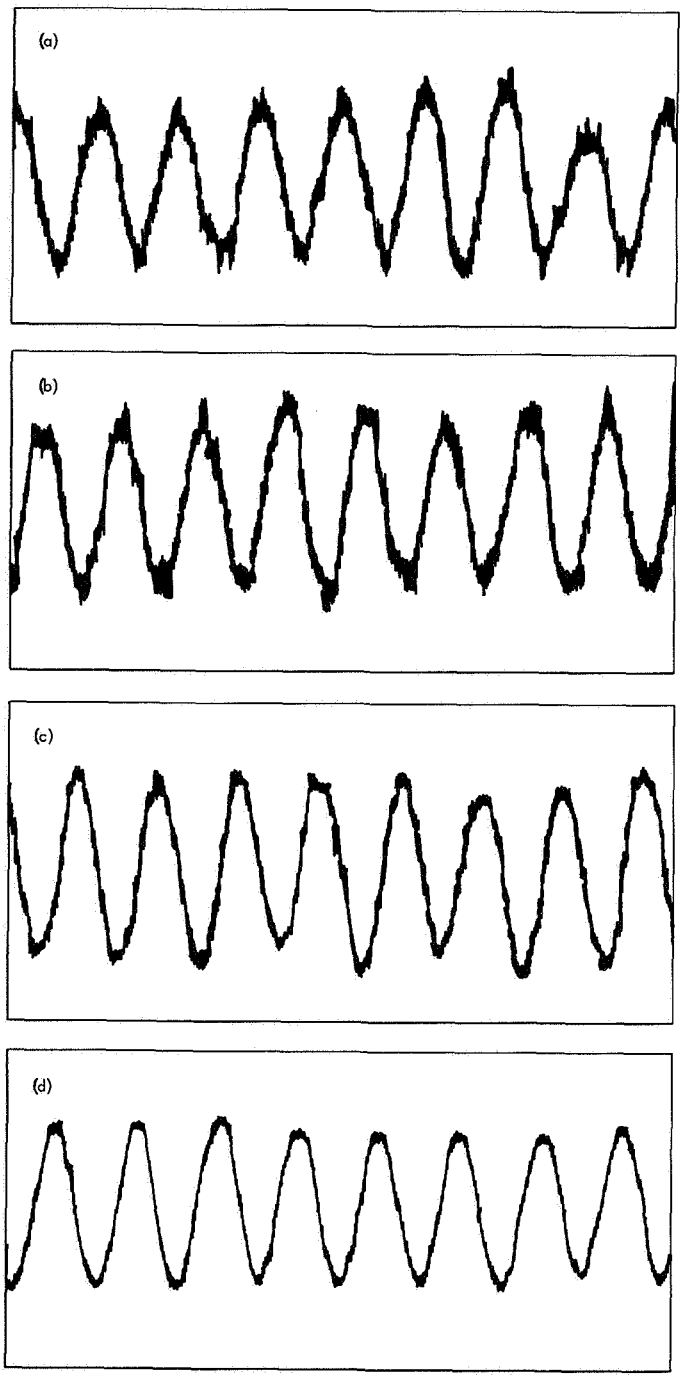

Fig. 14. Amplifier output waveforms for an input of 1 μV pp

Frequencies (a) 0.5 Hz, (b) 0.1 Hz, (c) 1 Hz, (d) 10 Hz; recorder sensitivity is 200 mV/cm.

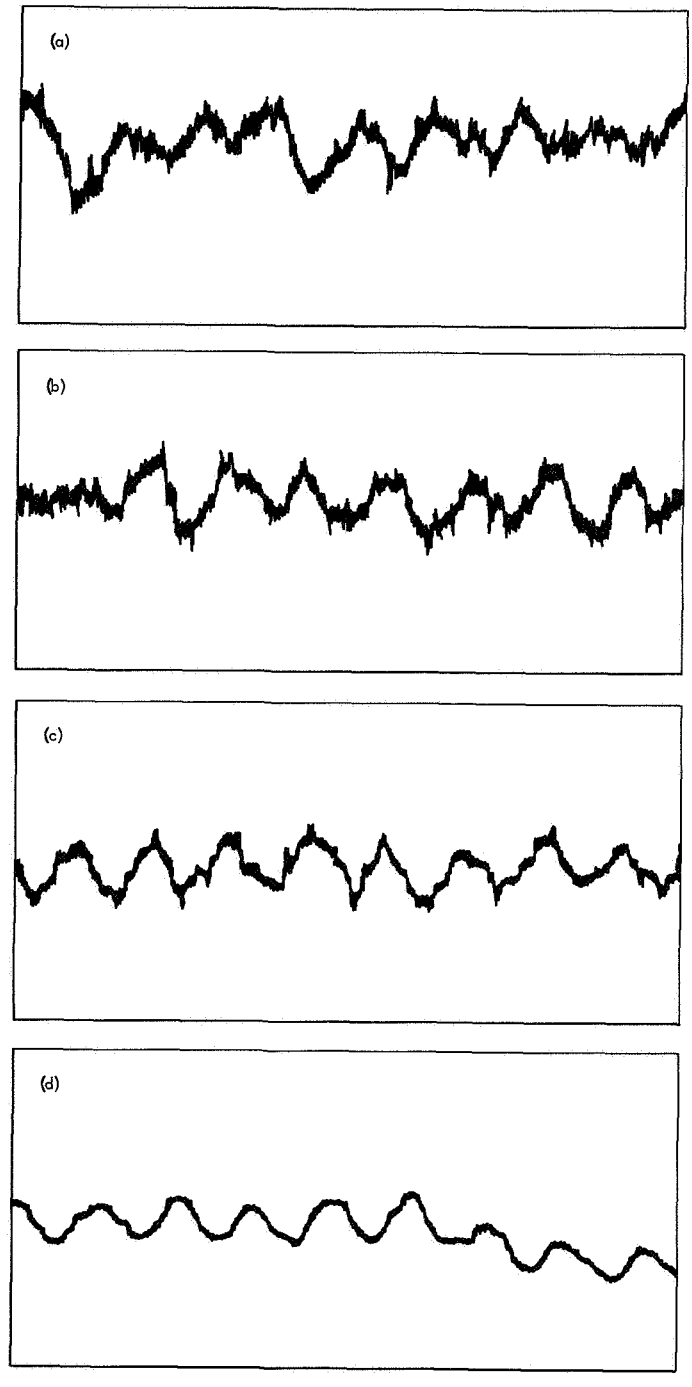

Fig. 15. Amplifier output waveforms for an input of ¼ μV pp

Frequencies (a) 0.25 Hz, (b) 0.1 Hz, (c) 1 Hz, (D) 10 Hz; recorder sensitivity is 200 mV/cm.

of accuracy and repeatability that is not attainable by the customary method of observation of meters or oscilloscope traces.

The *Surveyor* seismometer amplifier study program began in December 1965 as a result of an engineering evaluation of the *Surveyor* flight seismometer amplifier.

This evaluation and others before it showed that the seismometer amplifier circuit used in the *Surveyor* A-21A program was deficient in several areas. Consequently, an effort was initiated toward making a quantitative noise measurement and an improved amplifier design for this application.

Other advantages of the proposed redesign are: (1) reduced package size due to use of microcircuits where applicable, (2) instantaneous overload recovery, and (3) much improved temperature characteristics through the use of noncritical circuits and components.

The reasons for recommending development of a new amplifier are best understood when some of the design problems of the flight amplifier are considered. One of these problems is the use of two coupling capacitors preceding a chopper. These capacitors must have phenomenally low leakage currents, and matching of capacitor leakage current in the flight units is required.

It was considered that a lower noise figure could be obtained with a carrier-type (chopper, amplifier-demodulator) preamplifier rather than with a differential preamplifier as is used in the flight model amplifier. The original intention was to use dual-emitter chopping transistors, but the noise level turned out to be greater than expected. Consequently, junction FET transistors were substituted, and noise figures were measured which were approximately an order of magnitude lower than those of the flight amplifier. The "secret" of such a low noise level is in the use of chopper-drive transformers with FET transistors, something not usually done in FET chopping circuits because it is not necessary.

Figure 16 shows a block diagram of the prototype amplifier (note the provision for "center" demodulation). It was assumed that input chopping noise would be reduced by looking at the center of the chopped signal (Fig. 17), thus eliminating "spike" noise. However, in most tests it made no difference in the noise level, and in the final configuration it actually gave a 3-dB-higher noise level, as would be expected from the decreased

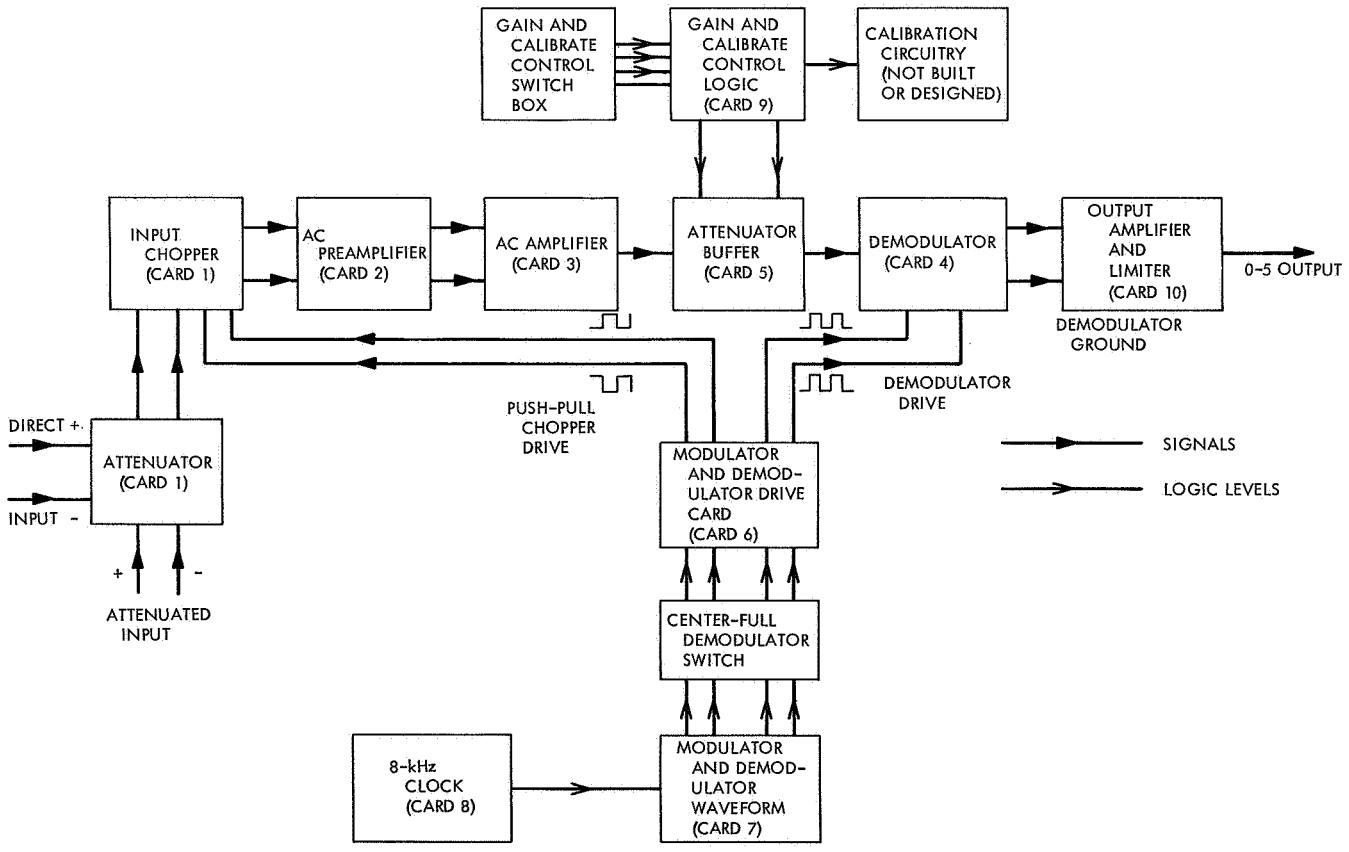

Fig. 16. Block diagram of development amplifier

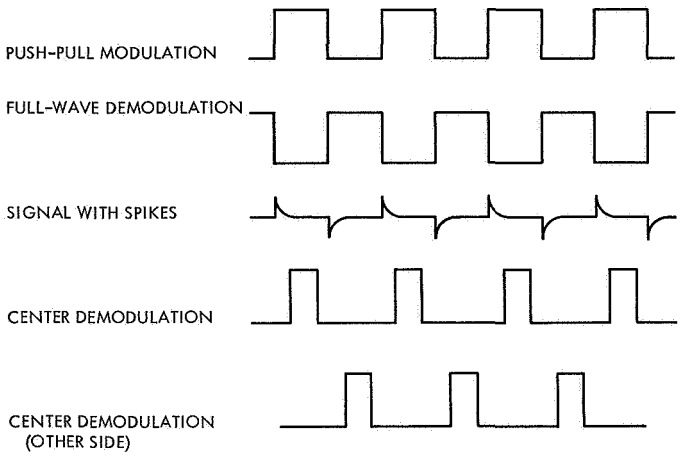

Fig. 17. Signal, modulation, and demodulation waveforms

signal-to-noise bandwidth ratio. The ac carrier amplifier is followed by a transistor-switched ladder-network attenuator. It is more satisfactory, circuitwise, to attenuate low-level ac signals than high-level signals.

Demodulation is accomplished by a full-wave transformer-coupled circuit. Full-wave demodulation is absolutely necessary for low noise performance, and care must be taken to ensure that the transformer is truly balanced (in this case the same bifilar-wound transformer is used in the flight amplifier). A half-wave demodulator would permit low-frequency noise in the amplifier to be added to the carrier frequency output.

The output of the demodulator is capacitively coupled to an integrated dc operational amplifier. The pass-band of this amplifier is from 0.05 to 20 Hz, and it also features automatic overload feedback protection, which means that it recovers almost instantly from the largest overload. The dc amplifier gain is about 200.

The modulation frequency is generated by a clock which drives a series of flipflops and gates. This circuitry is presently more complex than necessary because of the center demodulation feature.

The design of the input chopper or modulator is the most critical problem in the design of a low-noise amplifier. It was first decided that no input impedance-matching transformer should be used because of the extreme amount of shielding that would be necessary for good low-noise performance. An impedance-matching transformer would be desirable for two reasons: (1) the best noise figures in transistor circuitry are obtained at approximately 10,000-Ω source impedance (the spacecraft seismometer has an 860-Ω resistance), and (2) common-mode rejection problems are less severe. However, an adequately shielded input transformer might be too heavy and bulky for spacecraft application. Also, such a transformer might be microphonic at the very low signal levels being amplified. In practice, an ac preamplifier stage with a 4-dB noise figure was achieved, with a 1-kHz chopping frequency. This is only slightly higher than the noise at the most optimum source impedance.

Design of the preamplifier is influenced by the no-input-transformer concept. Because there is no transformer to aid in common-mode rejection, the input stage is similar in design to a dc differential input stage, including use of a constant-current generator to provide high common-mode rejection. The final configuration utilized a full-wave, four-field-effect transistor chopper. This arrangement doubles the effective signal input and almost doubles the signal-to-noise ratio.

2. *Random noise measurement.* Obtaining a low random noise level or noise figure was the most important objective of this design effort. (Random noise is noise due to thermal and other statistical phenomena, as opposed to nonrandom noise such as power-supply ripple, RF interference, etc.) The results of the random noise measurements are summarized in Table 2, which lists both the rms noise voltage (referred to input) and the noise figure.

A point that should be discussed in connection with the noise measurements is that the seismometer must be damped to 0.7 of critical damping by putting a 2000-Ω impedance across its output. This can be done either by a 2000-Ω resistor across the seismometer output terminals or by applying feedback to the amplifier so that its input impedance is 2000 Ω. The feedback method is the one used in the flight amplifier. It can be shown that there is a noise figure improvement of 3 dB with the feedback scheme, assuming 850-Ω seismometer impedance.

The feedback principle could be applied to the developmental amplifier as well, but common-mode rejection might become worse because of the reduced isolation between input and output. The improvement would probably not be enough to justify the additional circuitry.

Input chopping was originally tried with dual-emitter bipolar transistors. These transistors have a dc offset voltage of less than 50 μV when turned on. The noise figure obtained with the dual-emitter transistors, summarized in the following table, is significantly better than that of the flight amplifier in the range 0.02 to

Table 2. Random noise measurement results

Type	Noise voltage, rms (5–20 Hz), nV	Noise figure (5–20 Hz), dB	Noise voltage, rms (0.02–1.0 Hz), nV	Noise figure (0.02–1.0 Hz), dB
Breadboard flight-type amplifier (actual noise level)	218	23.7	117	30
Full-wave, 4 FET chopper developmental amplifier	29	5.74	17.5	12.8
Astrodata nanovoltmeter model 120	40	8.5	74.1	25.3
Half-wave, 2 FET chopper developmental amplifier	50	10.4	37	19.4
Half-wave, 2 dual-emitter chopper developmental amplifier	75	14	74	25.35
Breadboard flight-type amplifier corrected for 3-dB noise figure improvement due to internal damping	—	20.7	—	27

1.0 Hz by 6 dB and less significantly by 1.6 dB in the range of 5 to 20 Hz.

Later, junction field-effect transistors were employed in a two-transistor half-wave circuit as shown in the table. The noise levels are self-explanatory.

The final version, the full-wave, four-field-effect transistor chopper has far better noise characteristics than any other configuration that was tried. It should be noted that it has significantly lower noise figures in both frequency ranges than the Astrodata nanovoltmeter model 120. The Astrodata amplifier noise level was measured in order to provide a comparison with a commercial high-quality dc and low-frequency low-noise amplifier. The Astrodata uses a 400-Hz mechanical chopper.

Noise-level measurements in the region of 5 to 20 Hz were made with a Ballantine model 321 true-rms voltmeter preceded by a Krohn-hite model 330A bandpass filter set for 5 to 20 Hz.

Low-frequency noise measurements were made by sampling the amplifier output with a HP 5265A digital voltmeter and a HP 562A printer, mostly at a rate of 2 samples/sec. The amplifier output was filtered by the low-pass filter set to 1 Hz in order to eliminate sampling error. Most of the measurements were for 100 samples, which means that the lowest frequency sampled was $2/100 = 0.02$ Hz. These data were subjected to a Fourier analysis program on an IBM 1620 computer, which calculated the sine and cosine components of each frequency up to half the number of samples (50), obtained the absolute value of the sum of the square of the sine and cosine, and obtained the sum of these squares starting from the first harmonic. This last number, divided by 2, is the "power." To obtain the noise voltage in a bandwidth, say from 0.1 to 0.2 Hz, we subtract the power function at 0.1 Hz from that at 0.2 Hz, divide by 2, and take the square root.

Before the computer program performs the Fourier analysis, it makes a linear regression (least square fit) analysis which takes out the trend and obtains the total rms voltage. The program also takes the last total power function ($m = 50$), divides it by 2, and takes the square root. The Fortran statements for this program are shown in Fig. 18.

There is a weakness in the analysis program in that there was no compensation for overall system gain variation introduced by "rippled" frequency response of the Krohn-hite filter. This could easily be done by putting a delta-function input into the amplifier, and sampling the output in the same way as the noise measurement, but at a high level to minimize the effects of noise. The sampling rate and number of samples would be similar. A delta-function input is used because its transform gives the frequency response without any further calculation, unlike a step function.

3. Frequency response and common-mode rejection. Frequency response of the amplifier is from 0.05 to 20 Hz (3 dB points). Response is essentially flat from 0.2 to 10 Hz. The frequency response is determined primarily by the time constants in the dc output stage (Fig. 19). The low-frequency cutoff is determined by the time constants R_1C_1, C_6R_{14}, and C_2R_4. The high-frequency cutoff is determined by $C_3R_2R_3/R_4$, and also by C_1R_1 on the demodulator card (Fig. 20). Of course, the time constants in the ac amplifier have nothing to do with the frequency response. Common-mode rejection at 10 Hz was 95 dB.

4. Conclusion. An amplifier capable of much lower noise performance than the present *Surveyor* spacecraft seismometer amplifier has been designed and breadboarded. It is potentially more stable because circuit

```
      DIMENSION E(5,100)
      READ21,NA
   21 FORMAT (I4)
      READ20,((E(I,J),I=1,5),J=1,NA)
      PRINT21, NA
      PRINT20, ((E(II,JJ),II=1,5),JJ=1,NA)
   20 FORMAT(5E10.5)
      AA=5*NA
      ET=0.
      VT=0.
       FNB=(5*NA)/2
       CALL PLOT (101,0.,FNB,10.,5.,0.,.01,8...001)
      DO30 L=1,NA
      DO30K=1,5
   30 ET=ET+E(K,L)
      EM=ET/AA
      DO31 N=1,NA
      DO31M=1,5
   31 VT=(E(M,N)-EM)**2+VT
      VM=VT/AA
      S=SQRTF(VM)
      PRINT22,EM,S
   22 FORMAT (12H MEAN VOLT    ,E14.7,15HRMS NOISE VOLT    ,E14.7)
       ZL=NA*5
       ZM=ZL/2.
       RB=0.
       SR=0.
       DO 50 JB=1,NA
       DO 50 IB=1,5
       Z=5*JB+IB-5
       RB=RB+(E(IB,JB)-EM)*(Z-ZM)
       SR=(Z-ZM)**2   +SR
   50  CONTINUE
       BETA=RB/SR
       TREND=BETA*ZL
       ALPHA=EM-BETA*ZM
       TAR=0.
       DO 51 JC=1,NA
       DO 51 IC=1,5
       ZZ=5*JC+IC-5
       ES=ALPHA+BETA*ZZ
   51  TAR=TAR+(E(IC,JC)-ES)**2
       SIGMA2=TAR/ZL
       SIGMA=SQRTF(SIGMA2)
       PRINT 70
   70  FORMAT (7X,5HBETA    ,14X,5HTREND ,14X,5HALPHA ,14X,5HSIGMA)
       PRINT71,BETA,TREND,ALPHA,SIGMA
   71  FORMAT (4(5X,E14.7))
      NB=NA*5/2
       C2=0.
       DT2=0.
      DO41 MA=1,NB
      A=0.
      B=0.
      DO40 JA=1,NA
      DO40 IA=1,5
       U=IA+5*JA-5
       EL=ALPHA+BETA*U
       FMA=MA
       R=(U*FMA)/AA
      X=6.28318530*R
       DE=(E(IA,JA)-EL)*2./AA
       B=DE*SINF(X)     +B
       A=DE*COSF(X)     +A
   40  CONTINUE
       CA=C2
       C2=A**2+B**2
       C=SQRT(C2)
       DT2=DT2+C2
       XX=MA
       YY=C
       CALL PLOT (0,XX,YY)
   41  PRINT 24,MA,A,B,C,C2,DT2
   24  FORMAT (I4,5(5X,E14.7))
       DA=DT2/2.
       DT=SQRT(DA)
       PRINT 26,DT
   26  FORMAT (//15H SQ RT OF DT          ,E14.7)
       CALL PLOT (99)
       CALL PLOT (90.0.,0.)
      END
```

Fig. 18. Computer program

designs have been used which are not temperature-sensitive. It has been designed so that parts selection or matching will probably be unnecessary (as long as the parts have been screened). It is capable of being packaged in a considerably smaller space because much of the circuitry is integrated.

Much was learned about low-noise, low-frequency amplifier design. For example, it was found that a carrier amplifier employing a transformer drive and field-effect transistors as choppers should be used. It was also found that an input impedance matching transformer is not necessary, at least at impedance levels of approximately 1000 Ω. Another important design feature which was recognized is the need for a well-balanced demodulator.

It should not be inferred that the design and development effort for an adequate spacecraft seismometer amplifier is complete. The following "cleanup" effort will be required: removal of the unneeded logic and drive circuitry required for the center-demodulation; power-supply design; calibration circuit design; replacement of standard components with smaller equivalents (e.g., replacement of TO-18 outline transistors by TO-51's); examination of the possibility of using additional integrated circuits in place of discrete components.

E. Sensor Design

The short-period seismograph is basically a velocity transducer plus recorder, and its design is conceptually similar to that of the geophone, which has been used for years for terrestrial seismic work. The space application, however, imposes many new constraints on the design of the instrument.

The main requirements placed on the seismograph are as follows:

(1) Operation shall be nominal up to 15 deg of tilt of the spacecraft.

(2) Continuous operation shall be possible after nominal spacecraft touchdown (several lunar day–night cycles).

(3) The instrument shall have a nominal generator constant of 175 V sec/meter or more.

(4) The natural frequency (vertical, undamped) shall be 1.3 Hz ±20%.

(5) The instrument shall be sensitive to 1 mμ of motion at 1 Hz (corresponding to a velocity of 0.5×10^{-9} m/sec).

(6) The output signal shall be linear over the range of ½₀ to 20 Hz with a dynamic range of 35 dB and an analog output in the range of 0 to 5 V.

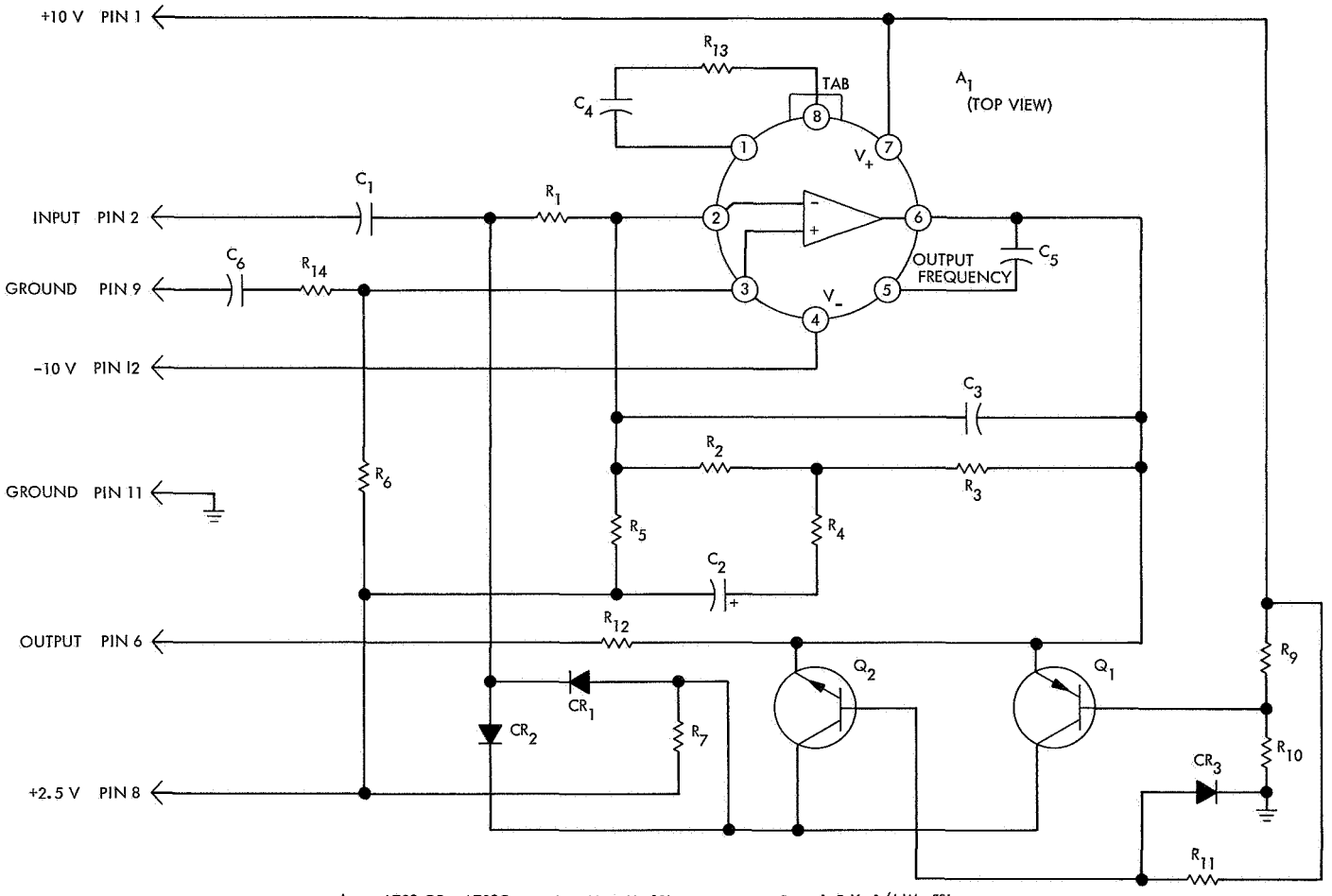

A_1, μA709 OR μA709C
C_1, C_2, 100μF
Q_1, 2N1132
Q_2, 2N910
CR_1-CR_3, 1N916
R_1, 36.5 K, 1%
R_2, R_3, 681K, 1%
R_4, 31.6 K, 1%
R_5, R_6, 10 K, 1%
R_7, 10 K, 5%, 1/4 W
R_9, 13.3 K, 1%
R_{10}, 10 K, 1%
R_{11}, 43 K, 5%, 1/4 W
R_{12}, 390Ω, 1/4 W, 5%
R_{13}, 1.5 K, 1/4 W, 5%
C_3, 470 pF
C_4, 4700 pF
C_5, 200 pF
C_6, 100 μF
R_{14}, 36 K, 1%

Fig. 19. Output amplifier card

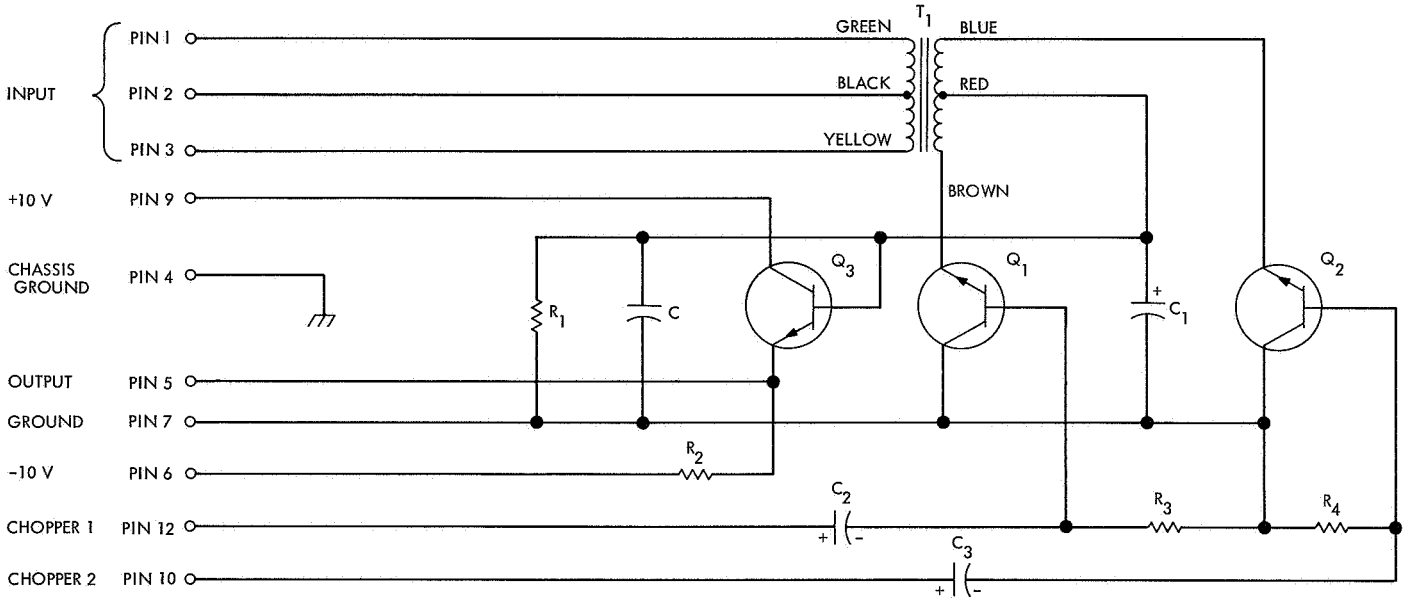

T_1, TRANSFORMER 1557 (DO-T36)
Q_1, Q_2, 2N914 (NOTE INVERTED CONFIGURATION)
R_1, R_2, R_3, R_4, 10 K, 5%
C_1, 4.7μF
R_1, 10 K, 5%
R_2, 10 K, 5%, 1/4 W
Q_3, 2N930
R_3, 9.1 K, 5%, 1/4 W
C_4, 4.7μF
C_2, C_3, 15μF, 20 V

Fig. 20. Demodulator card

It is convenient to separate the seismograph into two main parts: the sensor (and associated mounting hardware) and the electronic amplifier, which has been discussed above. The electronics, which operate satisfactorily over a smaller temperature range than the sensor, will be mounted in a thermally controlled compartment on the spacecraft. The sensor, which will tolerate large temperature changes, will be located wherever convenient on the spacecraft.

At the beginning of the program it was considered desirable to design the sensor for deployment to the lunar surface after the spacecraft had landed safely. Figure 21 shows the sensor in the stowed configuration; Fig. 22 shows the sensor in the deployed configuration, as it would look on the lunar surface. The sensor was to have been suspended on a cable from the tripod which was to be lowered to the surface. This approach was abandoned after it was realized that the achievement of a good coupling to the moon would be uncertain.

It was decided to connect the sensor directly to the spacecraft and to rely on the landing impact to develop a good coupling between the spacecraft foot pads and the lunar surface. The hardware developed to accomplish this task is shown in Fig. 23. Figure 24 is an exploded view of the seismograph. The seismometer consists of two subassemblies: the sensor (shown in exploded view in Fig. 25) and the mechanical support structure and thermal shell (shown exploded in Fig. 26).

The sensor consists of a spring-supported mass, moving relative to an induction coil, in which a minute output voltage is generated. The most efficient design for space applications dictates that the ratio of output voltage and sensor weight be maximum, which implies that the inertial spring-supported mass should be as large a part of the sensor mass as possible. Since a strong magnetic field (which is required to produce maximum sensitivity and a large generator constant) implies a massive magnet, it follows that the magnetic structure should be used as the floating inertial mass.

1. Magnetic design. Figure 27 illustrates the configuration of the magnetic flux paths within the sensor assembly. Alnico V-7 is used for the permanent magnet material, and the flux paths are completed through pole pieces of Hyperco 50. A–A is a plane of symmetry, and the upper and lower assemblies are identical insofar as flux paths are concerned. The position and polarization of the two magnets are such that when the upper and lower halves of the mass assembly are brought together, the normally fringing flux is pushed into an essentially uniform and radial field throughout the entire region from C to D.

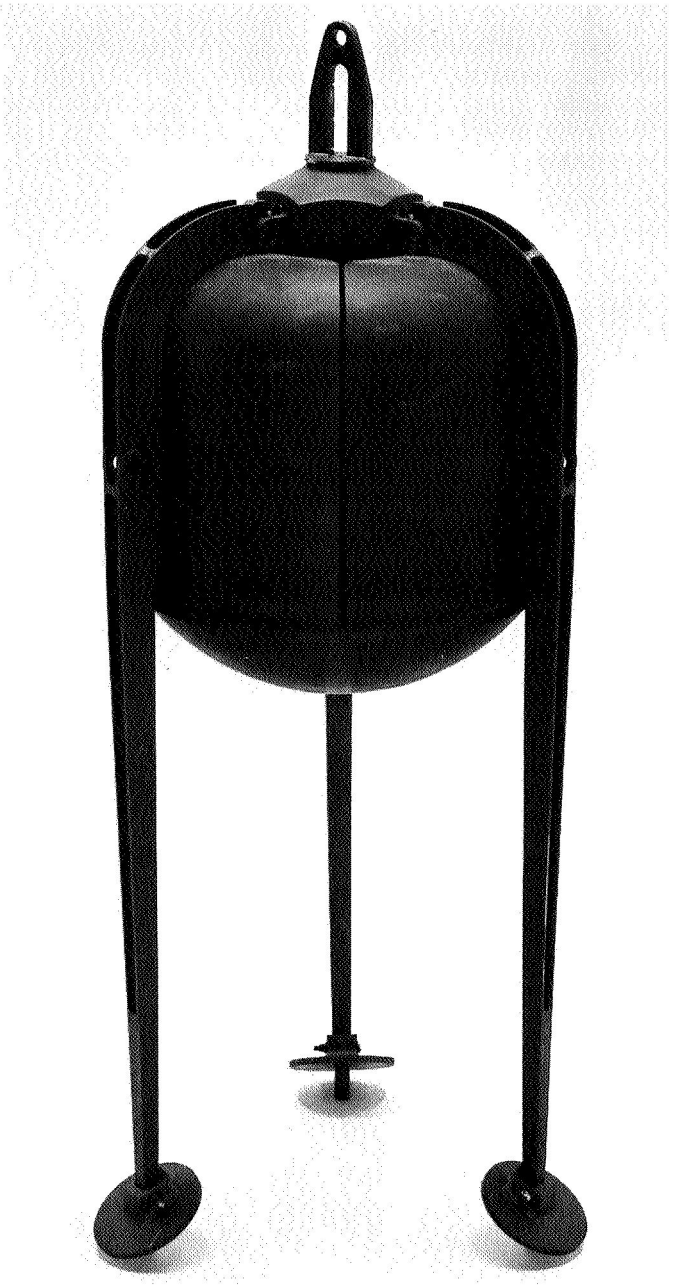

Fig. 21. Deployable seismometer in stowed configuration

The magnetization was performed by Ling–Temco–Vought.[2] Each magnet was saturated in the process, and

[2]Altec Lansing Corp., Anaheim, Calif.

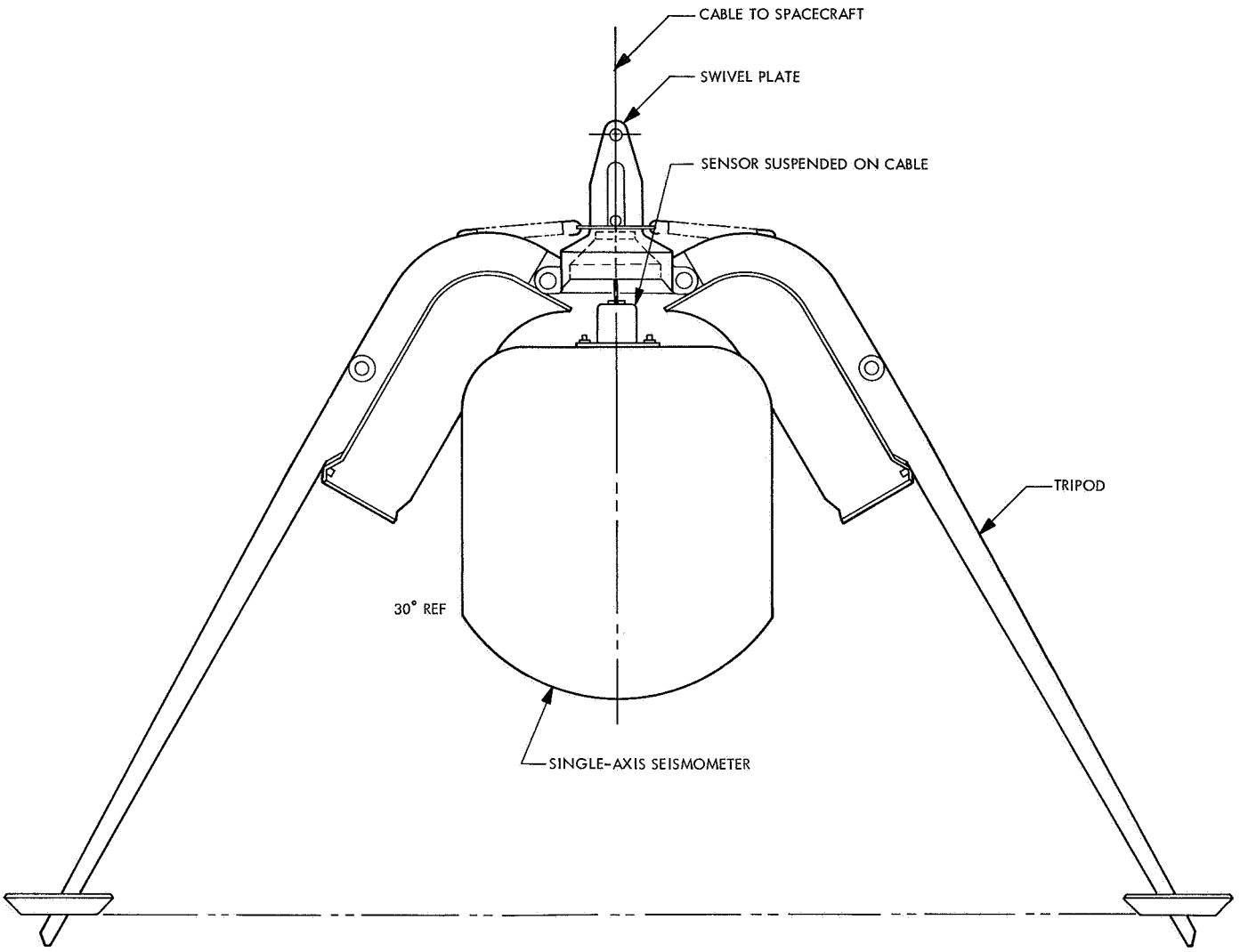

Fig. 22. Operational configuration

no cycling to increase stability was attempted. Extensive flux measurements were made prior to final assembly of the sensors, and typical results for magnets P4B and F-2 are shown in Fig. 28. The field strength appears to be quite uniform over the active gap length.

Results were generally consistent between various magnetic assemblies. Part of flight hardware F-4, after original magnetization, appeared to have abnormally low flux density. This section was demagnetized and remagnetized, after which it appeared to be of strength comparable to other units.

Some question exists regarding the magnetic properties and retention of full flux strength over extreme temperature cycles. This flux variation might occur in one of two ways:

(1) A temporary but reversible variation as a function of temperature.

(2) A permanent, partial demagnetization as a result of temperature cycling.

No physical experiment was performed specifically to investigate these possibilities. However, a brief literature review of the properties of Alnico V-7 revealed that no significant variation in flux strength should be expected. Flux variation over the temperature range covered by the Type Approval tests (-150 to $+180$°F) is expected to be of the order of 1% or less.

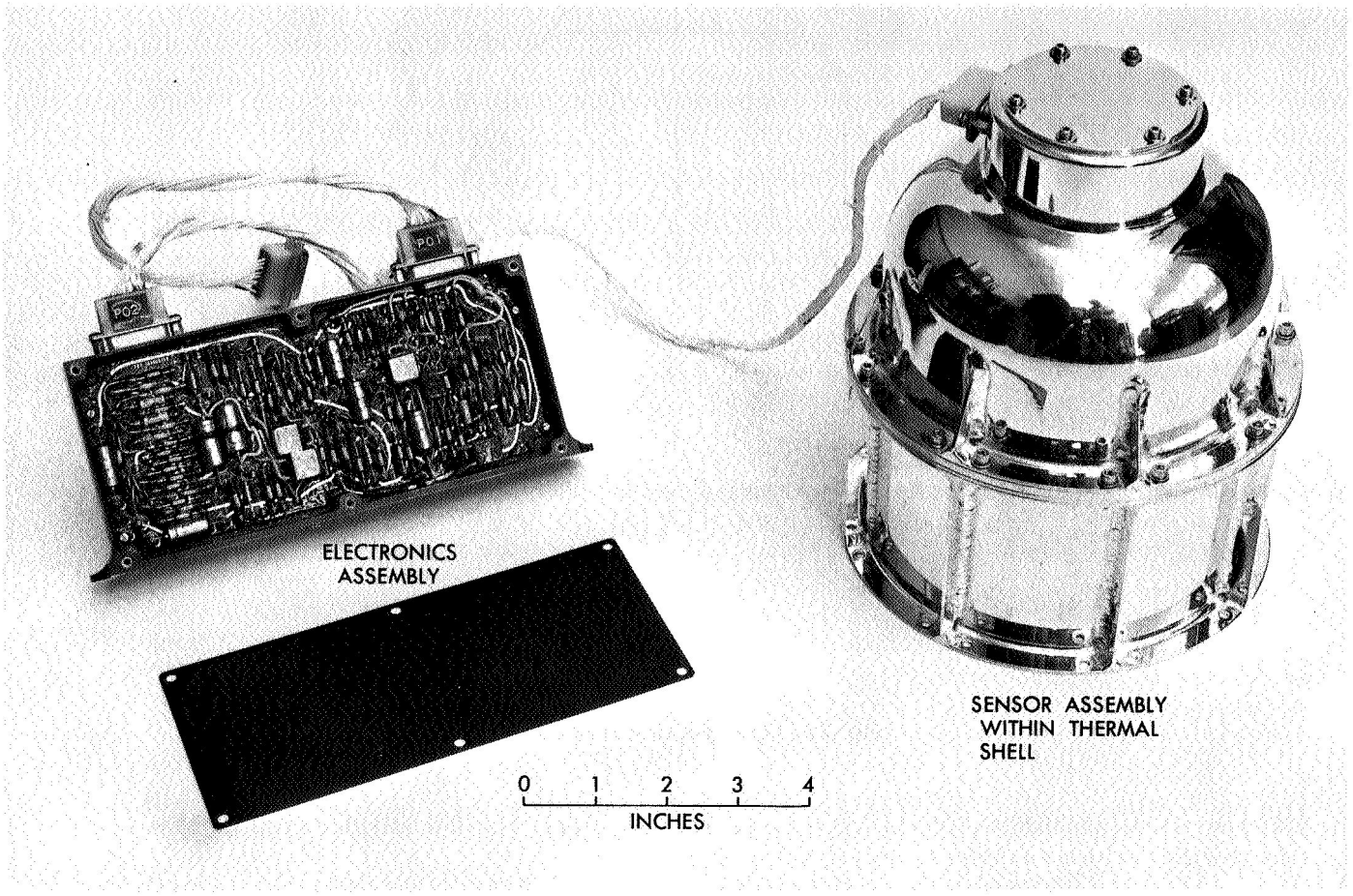

Fig. 23. Seismometer assembly

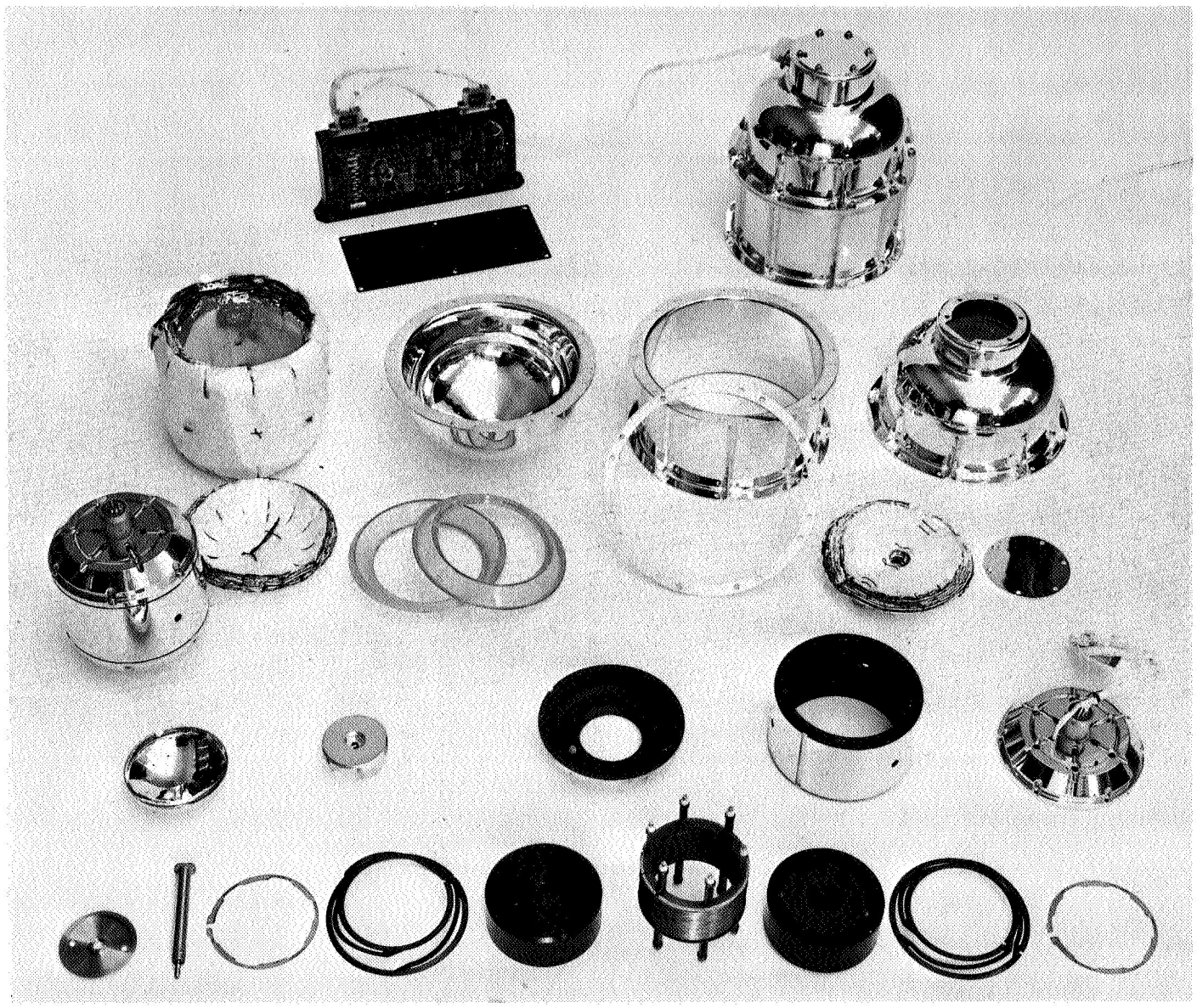

Fig. 24. Seismograph system, exploded view

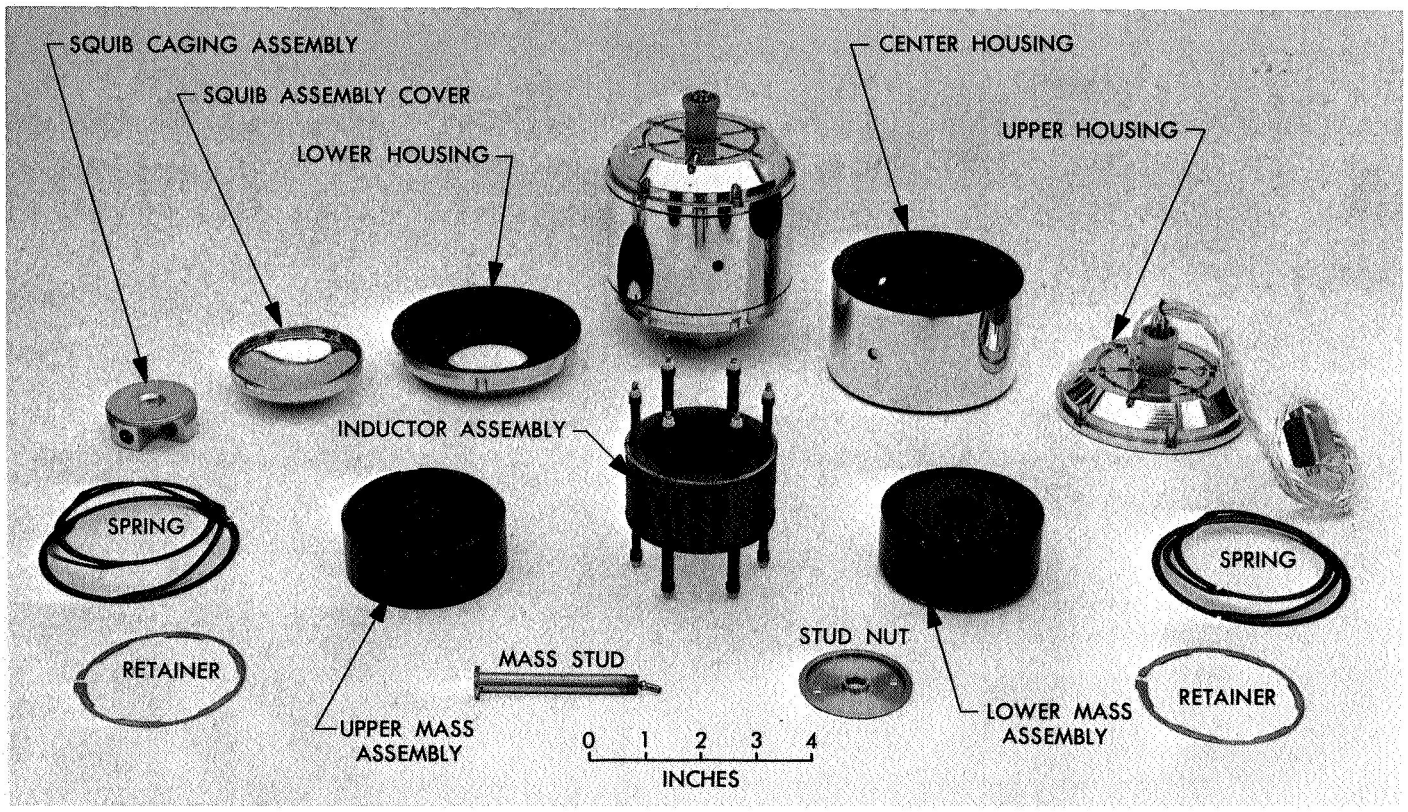

Fig. 25. Sensor assembly, exploded view

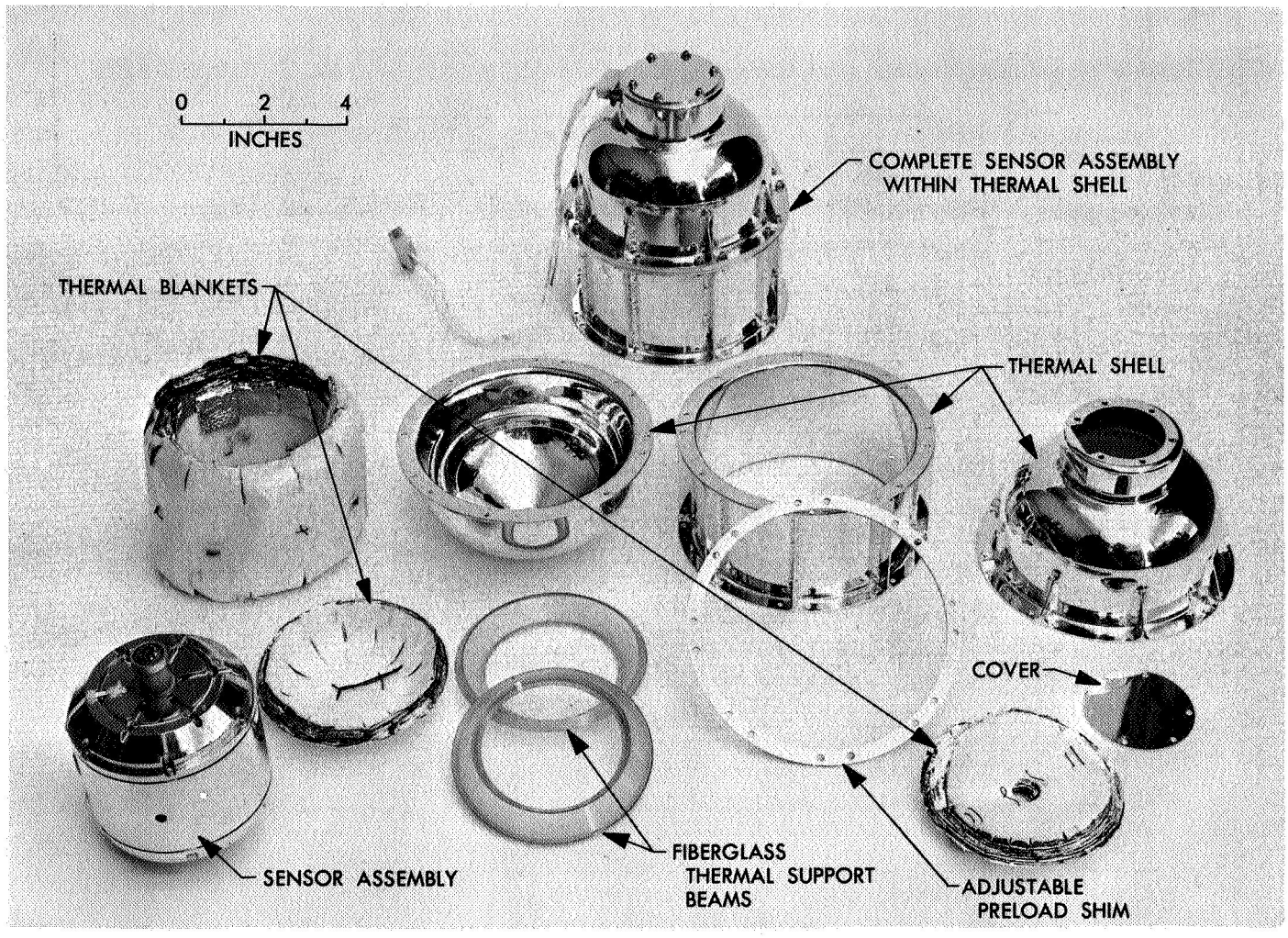

Fig. 26. Thermal and structural support system, exploded view

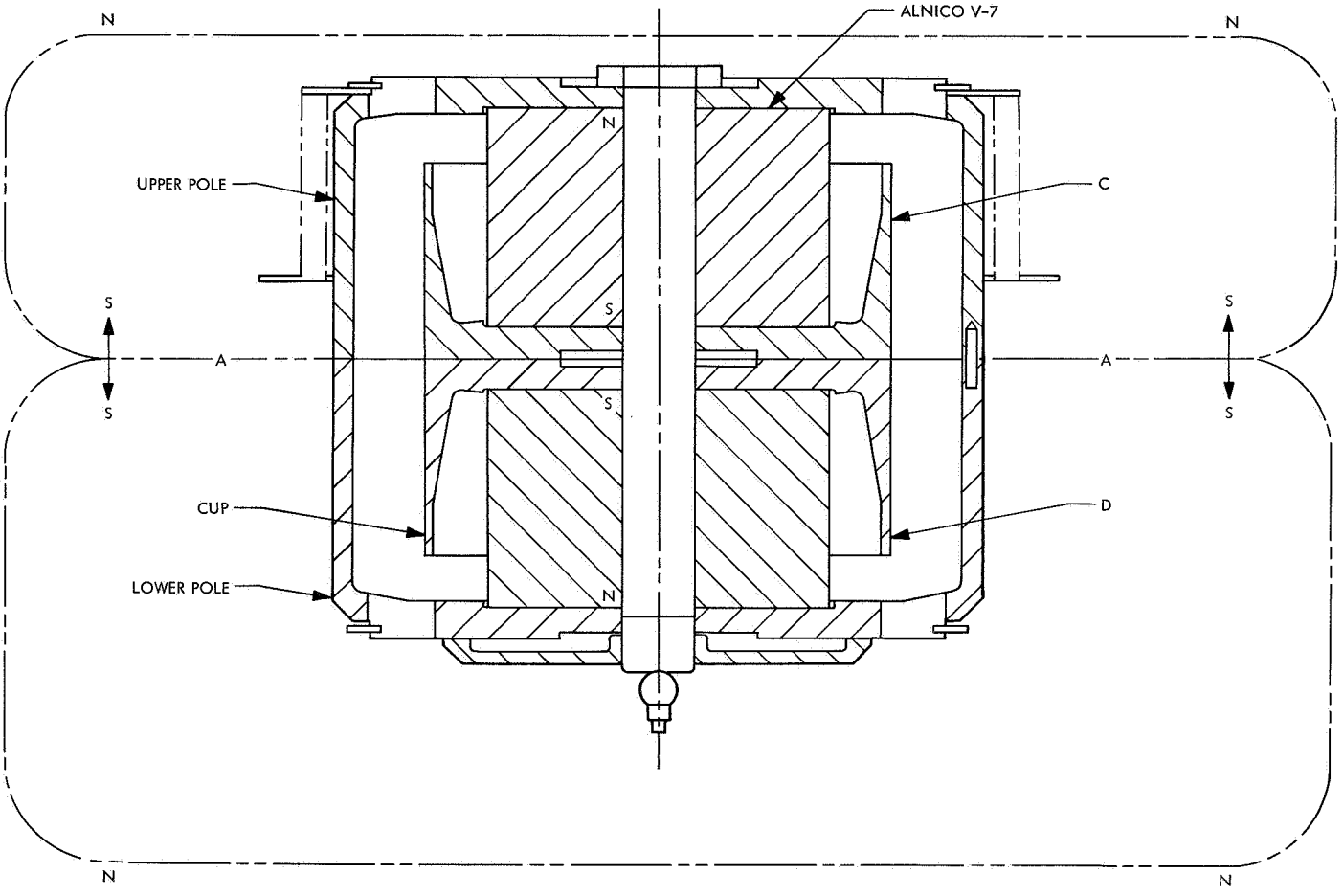

Fig. 27. Magnet cross section

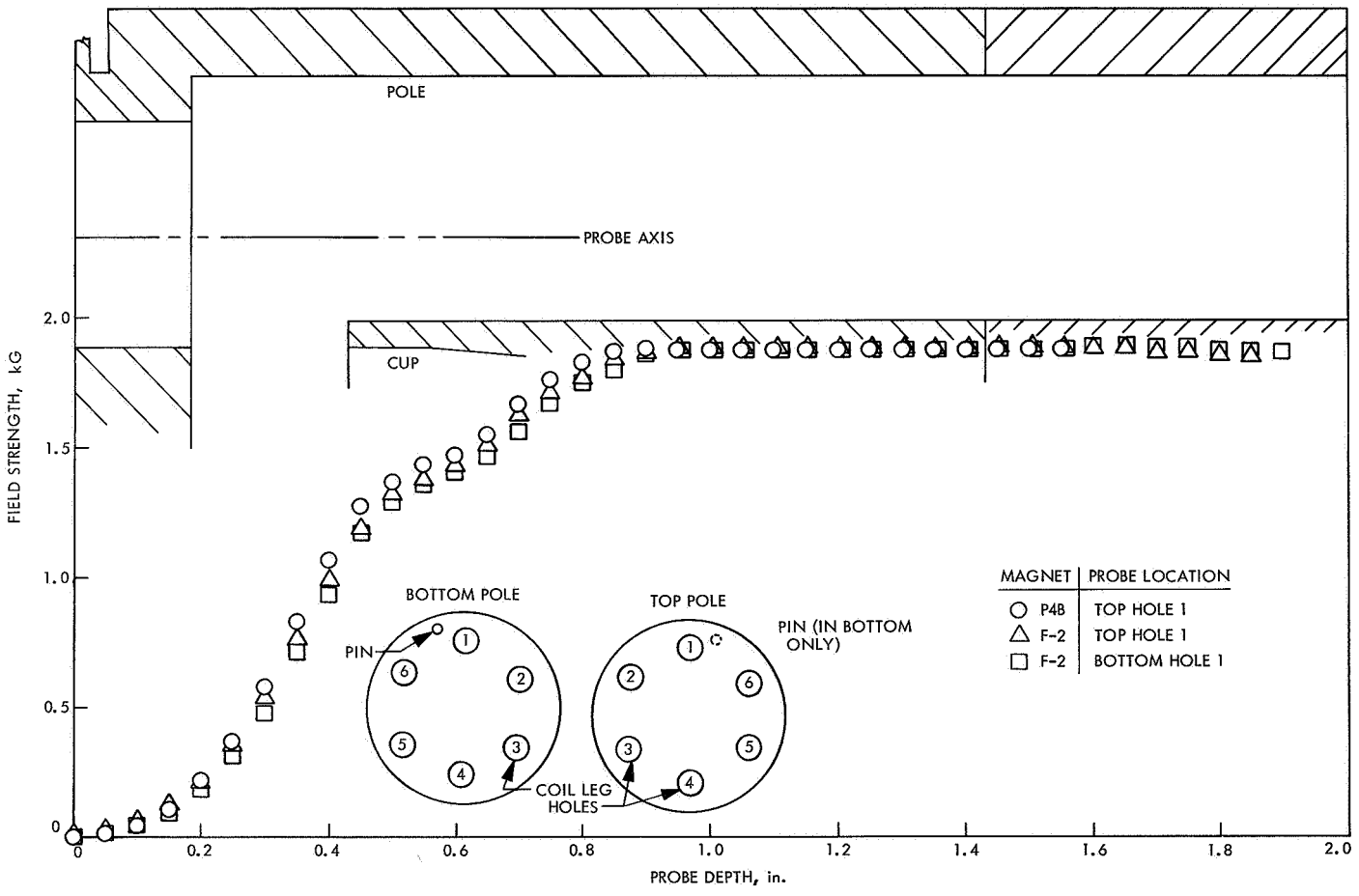

Fig. 28. Magnetic field map

The sensitivity and damping of the operating seismometer are both dependent upon flux density. It is essential that the flux density be as uniform as possible throughout the entire displacement range of the movable mass. In addition to the flux measurements, which were made directly, it is possible to determine the effective flux density, averaged over the length of the coil, by indirect methods. These measurements were made as a part of the Type Approval testing routine. Indications were that the effective flux density diminished by a maximum of 8% as the mass reached its terminal position against the lower stop within the sensor housing. A complete description of this analytical process is included in a subsequent section.

2. Transducer design. The sensor consists of an inertial mass which moves relative to a coil when a ground motion occurs (Fig. 29). The voltage generated can be written as

$$e = blv = gv \tag{1}$$

where

e = output voltage

b = magnetic field strength

l = length of wire in field

v = relative velocity of flux and wire

g = generator constant

It is evident from the above relationship that if e is to be a linear function of v, $b \times l$ should be a constant. It is also clear that for a given velocity v the maximum output voltage occurs when b and l are maximized, i.e., when the generator constant g is maximized. For the velocity transducer with damping provided by a resistive load, the generator constant can be written as

$$g = [4\pi f m (cdr)]^{1/2} \tag{2}$$

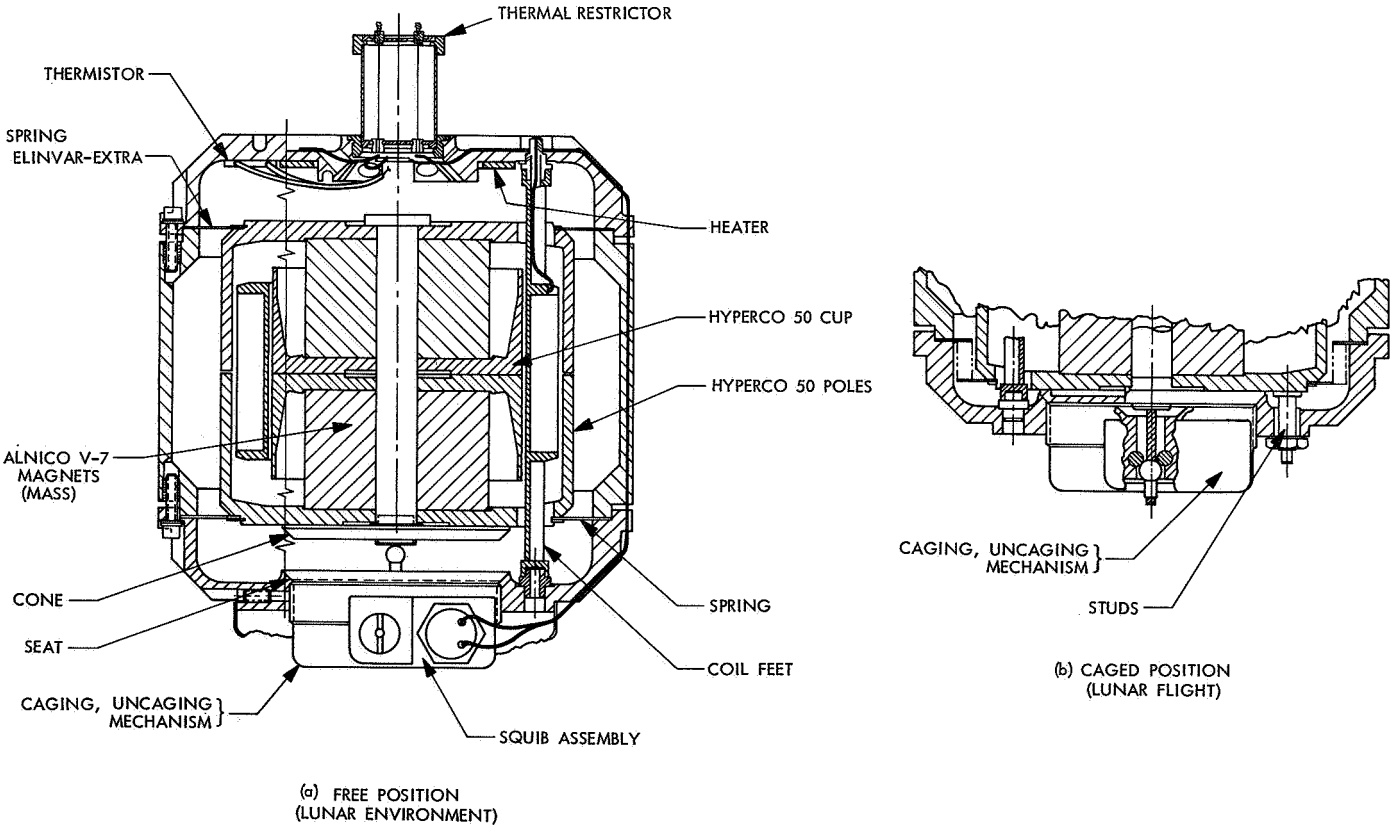

Fig. 29. Seismometer assembly

where

f = natural frequency of spring-mass system

m = spring supported mass

cdr = total circuit resistance for critical damping

It can be seen from Eq. (2) for constant resistance and natural frequency that the generator constant increases with $(\text{mass})^{1/2}$. Hence for high sensitivity it is necessary to use as large a mass as possible. Since it is desirable from Eq. (1) to make the flux density b as large as possible (for a given length of wire l), and since the flux for a permanent magnet varies roughly as the mass, it is desirable to let the magnet be the moving mass and the coil the stationary member. The resulting configuration for the *Surveyor* seismometer can be seen in Figs. 29 and 30. The magnet is designed to provide a uniform radial flux within a closed magnetic shell with very little leakage flux. In addition to providing an efficient design, this configuration also satisfies the spacecraft requirement that the stray magnetic field be less than 1000 gamma at a distance of 4 ft from the sensor. The pole pieces are perforated with six holes on each end to allow the coil to be supported on six feet by the housing (Fig. 29).

The magnets, the cups, and the pole pieces are clamped together with a stainless-steel stud which encloses the caging cable. The cable is shown in the uncaged position in Fig. 29a and in the caged position in Fig. 29b. The mass (magnets) is centered by a conical seat and is supported by four studs which are adjusted to prevent rotation of the mass during vibration.

The mass is restrained by the caging mechanism during the transit phase of the mission and is released when the squib-fire circuit is energized after touchdown. The squibs move two pistons (two for redundancy) to release the ball and cable, allowing the mass to return to its

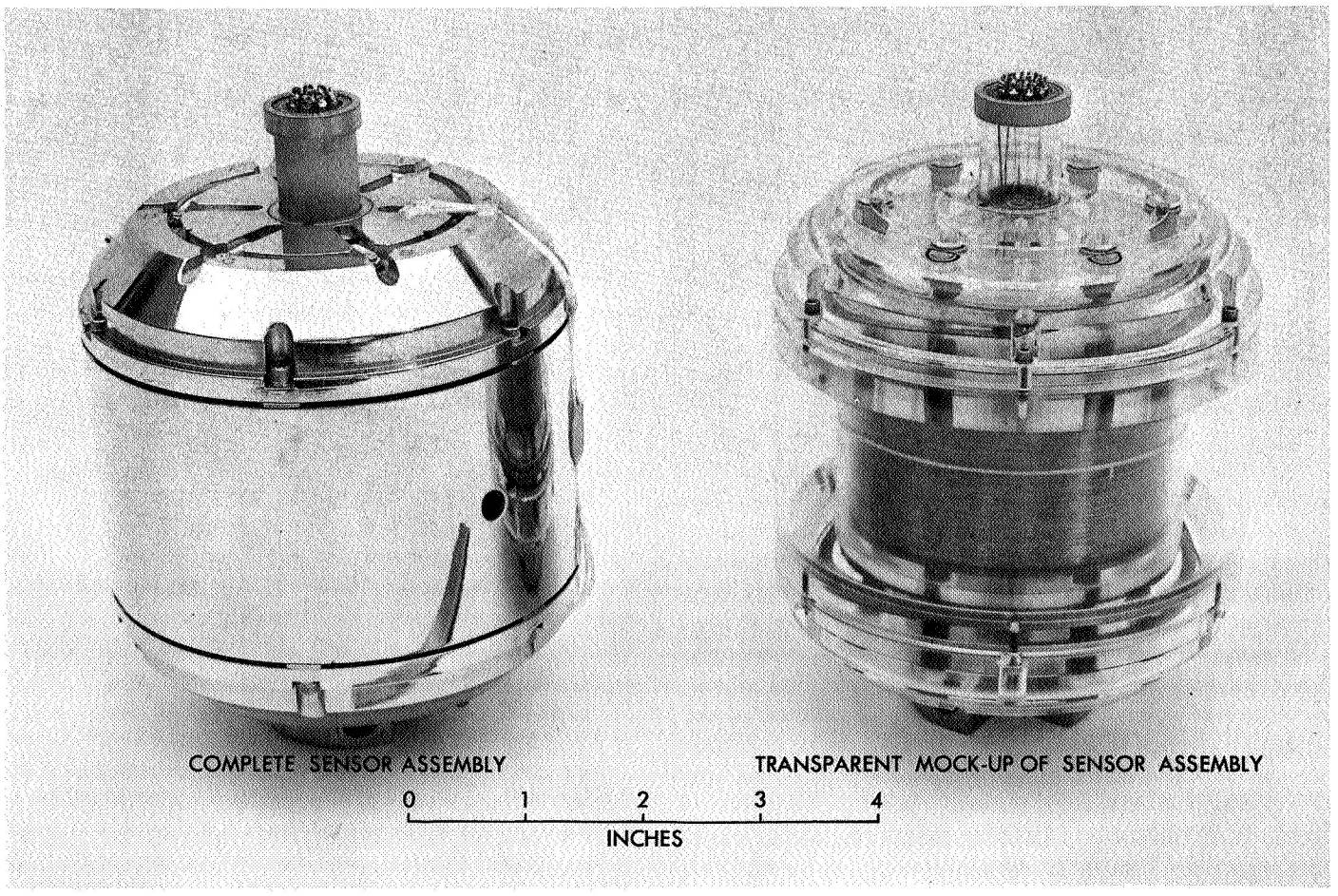

Fig. 30. Sensor assembly

nominal equilibrium position as shown in Fig. 29a. The ball and cable are held inside the mass by a spring. The tension in the cable required to withstand the vibration loads is obtained by adjusting the position of the squib assembly in the main housing. A cross section of the squib-operated mass release mechanism is shown in Fig. 31.

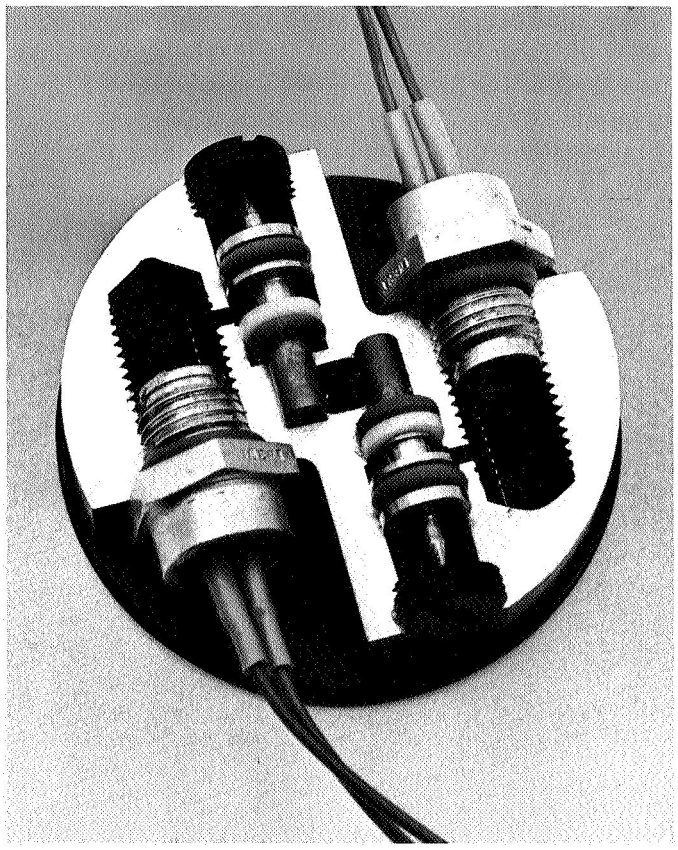

Fig. 31. Cross section of mass release mechanism

For minimum weight, the coil form (bobbin) is made from magnesium (as is the housing) and is cut lengthwise to increase the resistance to the flow of eddy currents in the bobbin. A fiberglass spacer is bonded into the slot to restore the bobbin to its original strength, stiffness, and shape. All except one of the legs of the coil form are insulated from the housing, again to avoid continuous current loops. The coil contains a calibrate coil of 200 turns and a bifilar winding of 2550 turns. The wire, which is AWG 33, Formvar Bondeze,[3] was layer-wound and solvent-bonded after completion of the winding operation. Figure 32 shows the completed coil.

[3]Phelps Dodge Manufacturing Co.

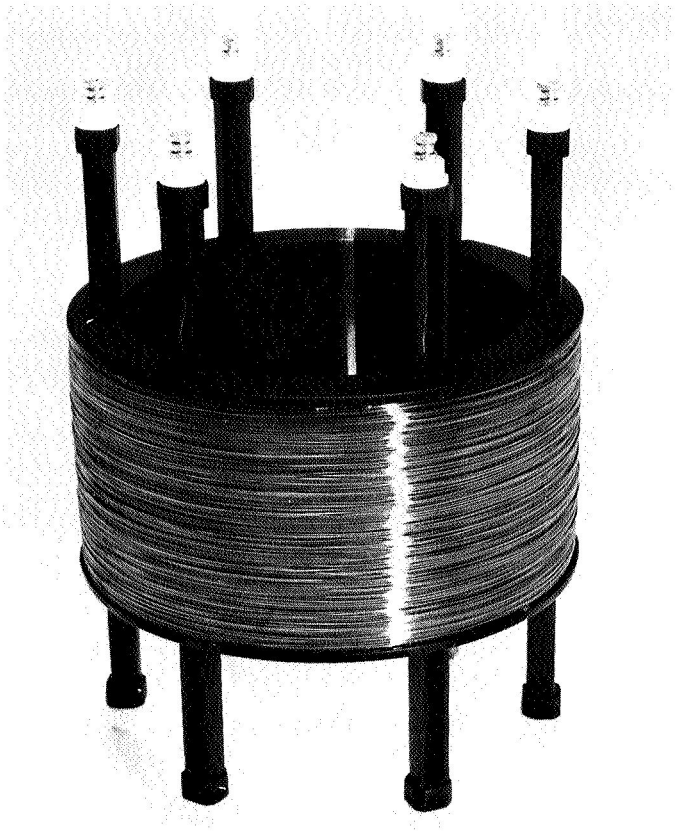

Fig. 32. Seismometer coil assembly

3. Spring design. The mass (magnet assembly) is supported by two flat springs which are designed to provide a nominal natural frequency of 1.3 Hz. A more compact instrument design can be achieved with this type of spring than with a simple helical spring. Figure 33 shows one spring in its unloaded configuration. The spring blank is eloxed from sheet stock, stretched, and heat-treated.

The load-deflection curve for the seismometer spring is nonlinear and is of the form shown in Fig. 34. The design problem, to provide the proper load-deflection curve, reduces to the problem of selecting the blank thickness, beam width, preform (length under no load) material, and heat treatment. The material selected must satisfy the temperature requirements, and ideally should have the same load-deflection curve for all temperatures within the operating range (-250 to $+250$°F, lunar environment). The initial seismometer design called for the use of beryllium–copper springs clamped tightly on their outer rims by the magnesium housing. But because of anticipated thermal problems it was decided to: (1) develop new springs which would minimize sensitivity to temperature; (2) unclamp the outer rings of the

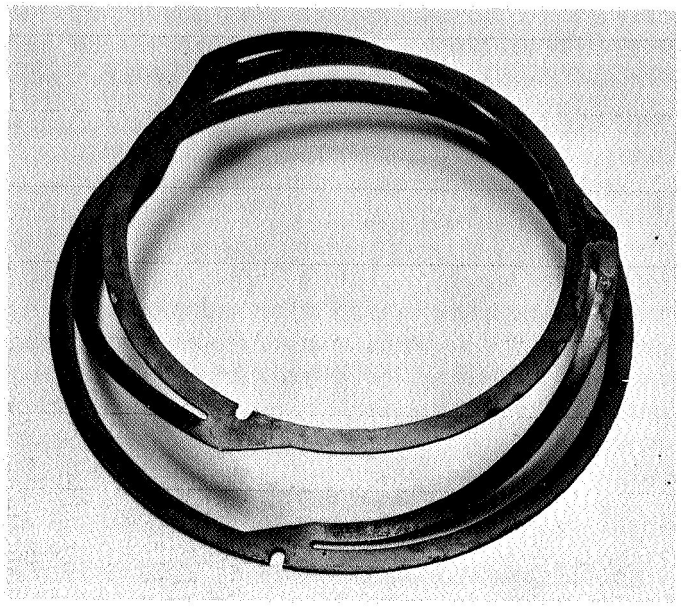

Fig. 33. Seismometer support spring (2 used)

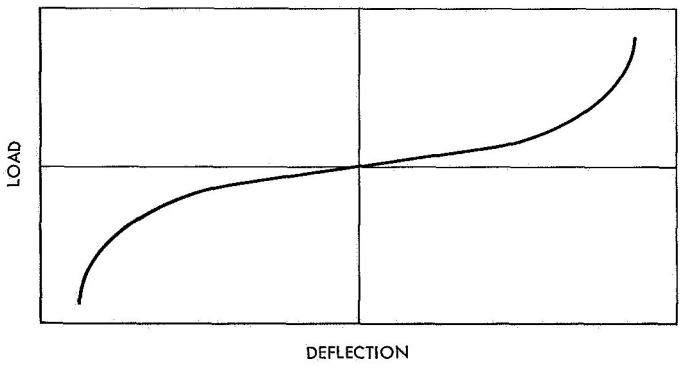

Fig. 34. Load vs deflection for the seismometer springs

springs; and (3) develop a thermal control system for the sensor. (The thermal control design is discussed subsequently.)

Elinvar-Extra was chosen for the spring material because its thermal coefficient of elasticity can be adjusted by heat treatment, and it is possible to produce a spring which, over a limited temperature range, has a modulus of elasticity-vs- temperature curve with a positive, zero, or negative slope.

The curve of spring load vs deflection was approximated by a cubic equation whose coefficients were obtained from the spring specifications. It has been assumed that the required load-carrying capability is achieved at the inflection point of the characteristic equation. If this point is taken as the origin of the deflection measurements, the cubic approximation can be written as

$$F = Px^3 + Qx^2 + Kx + W$$

where $F\big|_{x=0} = W$ = mass weight in lunar gravity (273 g), $(dF/dx)\big|_{x=0} = K$, and K is thus defined by the natural period requirements of the spring characteristic specifications (1.3 sec ±20%).

The symmetry of the spring constant (dF/dx) with respect to $x = 0$, observed in experimental deflection vs load curves, requires that $Q = 0$.

The spring characteristic requirement limiting natural period variation with tilt puts an upper limit on the value of P. If this limiting value of P is used, the worst acceptable characteristic with regard to period degradation is obtained. For $P = 0$, the worst possible condition of deflection vs tilt and temperature is realized (i.e., linear spring).

A plot of the cubic equation gives deflection vs load (similar to Fig. 34) for the nominal natural period of 1.3 sec (curves could also be obtained for the extreme conditions of ±20%). One can take the slope at various loads and substitute into the period equation $T_o = 2\pi(M/K)^{1/2}$, where K is the slope and M is the mass, in appropriate units. A plot of period vs load can now be drawn.

It should be noted that tilt is equivalent to a rotation of the gravity vector or simply a variation in weight. Also, using experimentally determined spring curves (Figs. 35, 36) at various temperatures (for Elinvar-Extra and beryllium–copper), one notes that a change in operating temperature is equivalent to a change in weight-carrying capability or simply a translation of the curve along the load axis.[4]

Based on this observation one can calculate the natural period at various temperatures and obtain the curve of Fig. 37. The curves are for a nominal 1.3-sec-period and for the two spring materials, beryllium–copper and Elinvar-Extra.

Similarly, the variation of natural period and mass position can be established for any operating temperature. This relationship has been plotted in Fig. 38.

[4]This is at least a good first-order approximation.

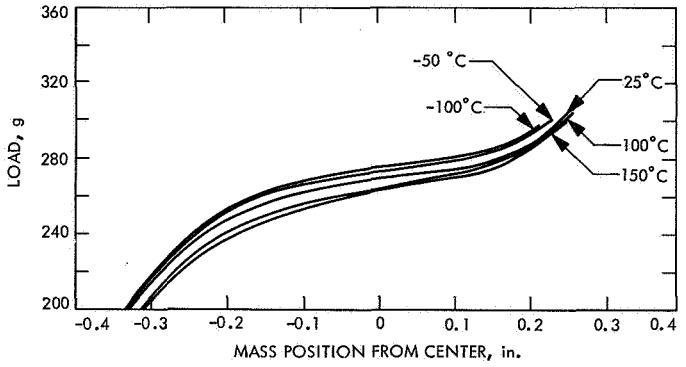

Fig. 35. Beryllium–copper spring deflection as a function of load and temperature (clamped outer ring)

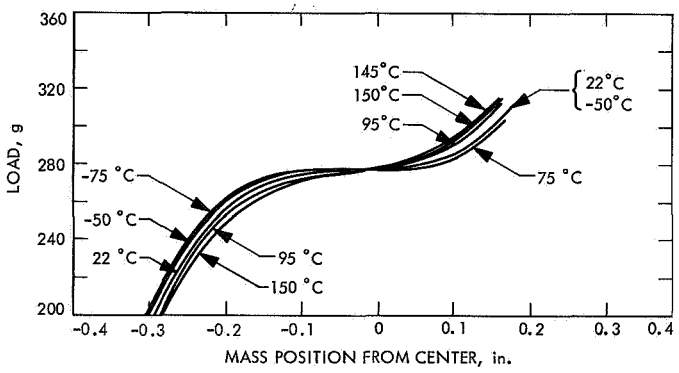

Fig. 36. Elinvar-Extra spring deflection as a function of load and temperature (clamped outer rings)

Curves labelled "tilt vs division" which are provided in Figs. 37 and 38 show the effect of instrument tilt on the equilibrium natural period. To obtain the period for a given tilt, read the division for the tilt angle and lay this off toward the left on the temperature axis. Start at the operating temperature and count off the divisions using the upper graduations (tilt divisions).

On the basis of this analysis, both materials, if within specifications, will provide an operative lunar instrument for extreme operating conditions (−100°C and 15 deg tilt). However, temperature-induced variations of natural period affecting the overall instrument response are much bigger with BeCu than with Elinvar-Extra. For a typical spring set, the natural period may vary from 1.3 to 0.77 sec for a BeCu set, compared to 1.3 to 1.16 sec for Elinvar-Extra, whenever the temperature deviates 100°C from the design center.

Figure 37 shows the results of tests of a beryllium–copper spring set; Fig. 38 shows the results for a pair of Elinvar-Extra springs. In both tests, the springs are clamped in the housing. It is evident from the test data that the housing is deforming the springs radially as the temperature is raised.

There are two solutions to this problem of relative thermal expansion of mating materials: (1) to fabricate the housing and the springs from the same material, (2) to unclamp the springs so that the spring and the housing can expand relative to each other without loading the springs radially. To avoid hysteresis losses in the spring mounting, it would appear better to clamp both the inner and outer rings. However, for terrestrial seismometers of similar design, the inner ring of each spring is left floating. More repeatable results are obtained with this approach.

For the lunar seismometer (*Surveyor*) it was decided to let the outer ring float, since matching the housing material with the Elinvar-Extra springs would produce a large weight penalty. Data for a set of beryllium–copper springs (inner and outer rings unclamped) tested over the temperature range of 100 to 150°C are presented in Fig. 39; similar data for a set of Elinvar-Extra springs are presented in Fig. 40. There is a definite gain obtained by using Elinvar-Extra springs for this application.

The remainder of the spring problem is concerned with the geometric design and material heat treatment required to produce springs which will support the correct mass and have the desired load-vs-deflection relationship. Because of the difference in earth and moon gravity and because of the anticipated difficulty of calibrating the lunar seismograph on earth, it was decided to develop earth springs in parallel with the lunar spring development so that the sensor could be calibrated on earth using earth springs.

The seismometer uses two springs to suspend the mass and to control its motion to be rectilinear and parallel to the axis of the inductor. For large deflections, the mass has a small rotation about the coil axis, but for small deflections of the size expected the rotation is negligible. It is desirable to have a uniform spring constant over the range of travel of the mass as shown between *A* and *B* in Fig. 41, with the spring in a plane configuration at the nominal load support point *C*. The springs can be designed to provide a long, approximately linear region in the range *A* to *B*. Since two springs are required for kinematic constraint, it would seem logical to make the springs identical so that each would carry half the load and have identical load-vs-deflection curves

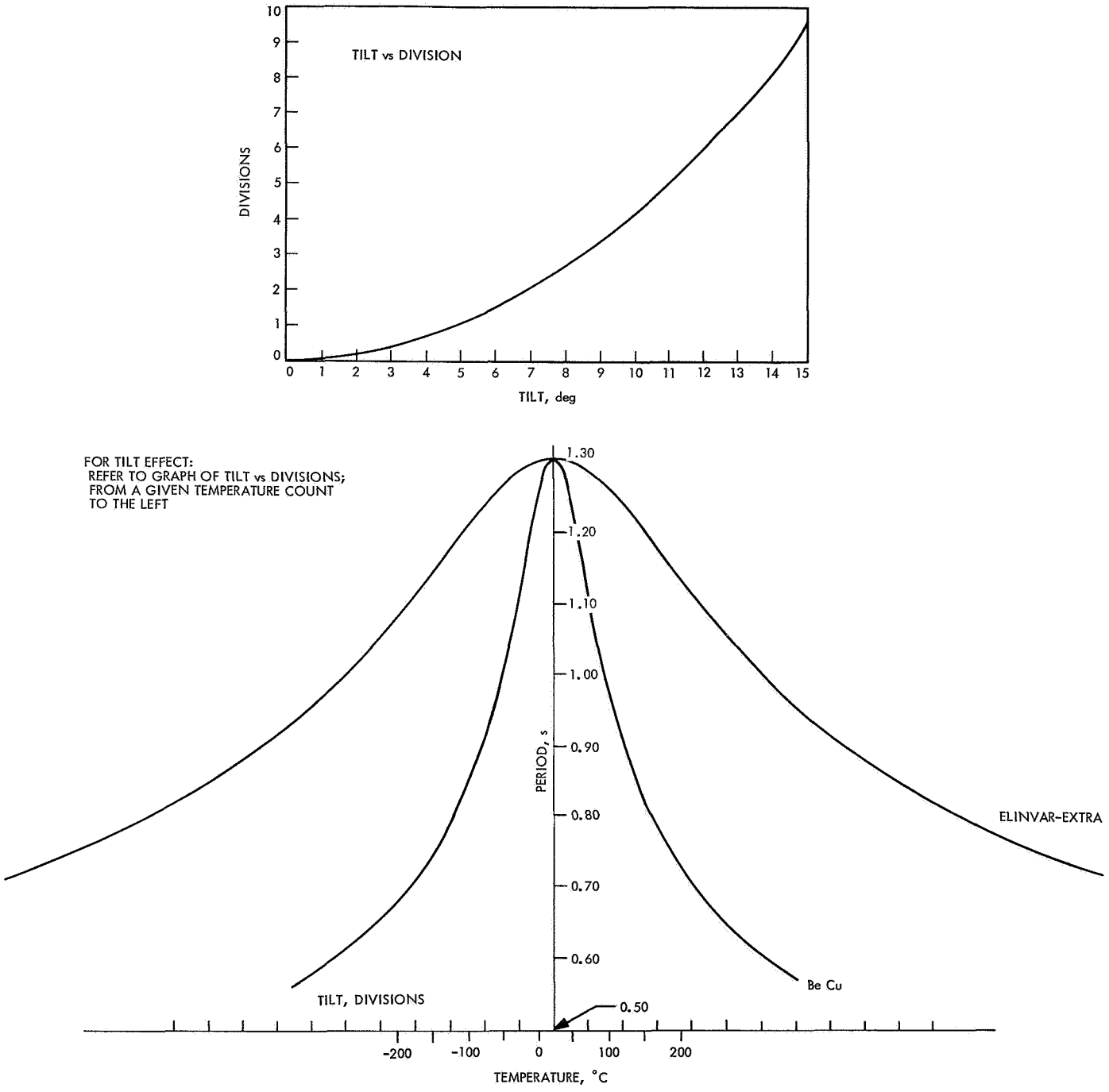

Fig. 37. Period vs tilt and temperature

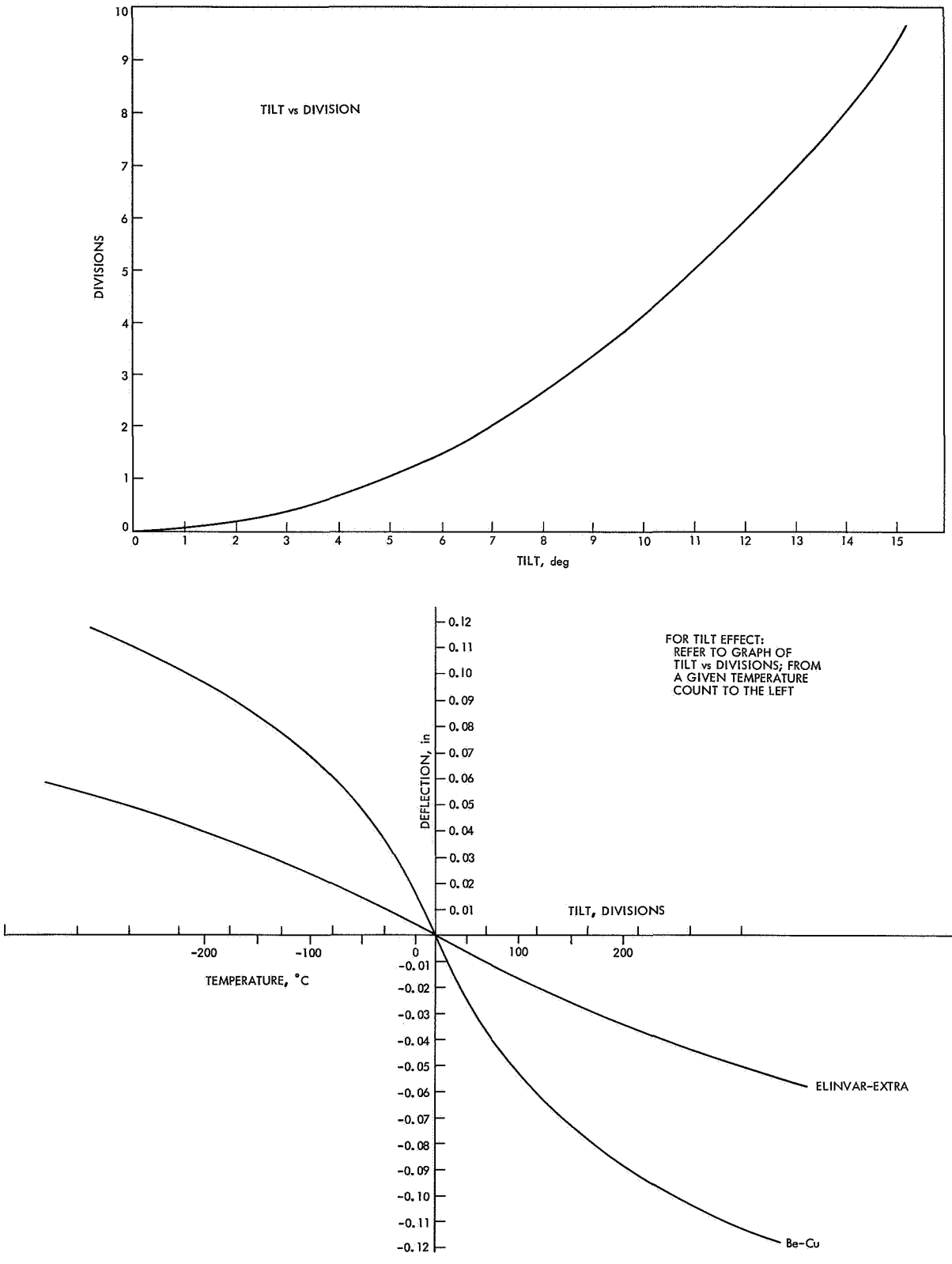

Fig. 38. Deflection vs tilt and temperature

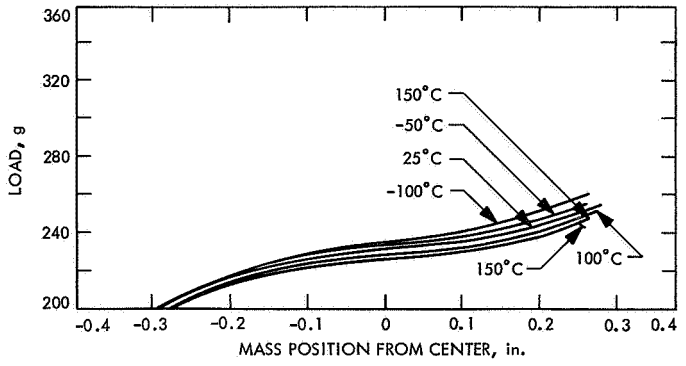

Fig. 39. Beryllium–copper spring deflection as a function of load and temperature (outer rings unclamped)

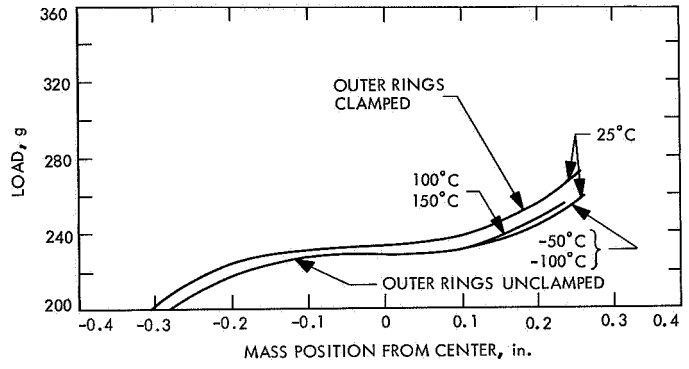

Fig. 40. Elinvar-Extra spring deflection as a function of load and temperature with unclamped rings

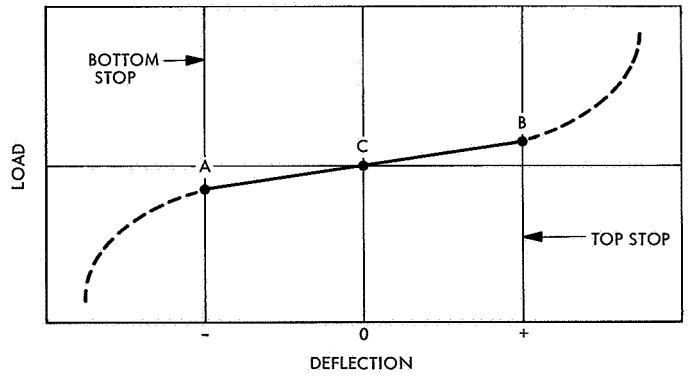

Fig. 41. Ideal spring deflection as a function of load

which could be added (by superposition) to produce the final identically shaped curve. However, practically, it is easier to get the low natural frequency and high mass support by making one spring unstable (Fig. 42a) and the other stable (Fig. 42b) so that when added together the result is the curve of Fig. 42c.

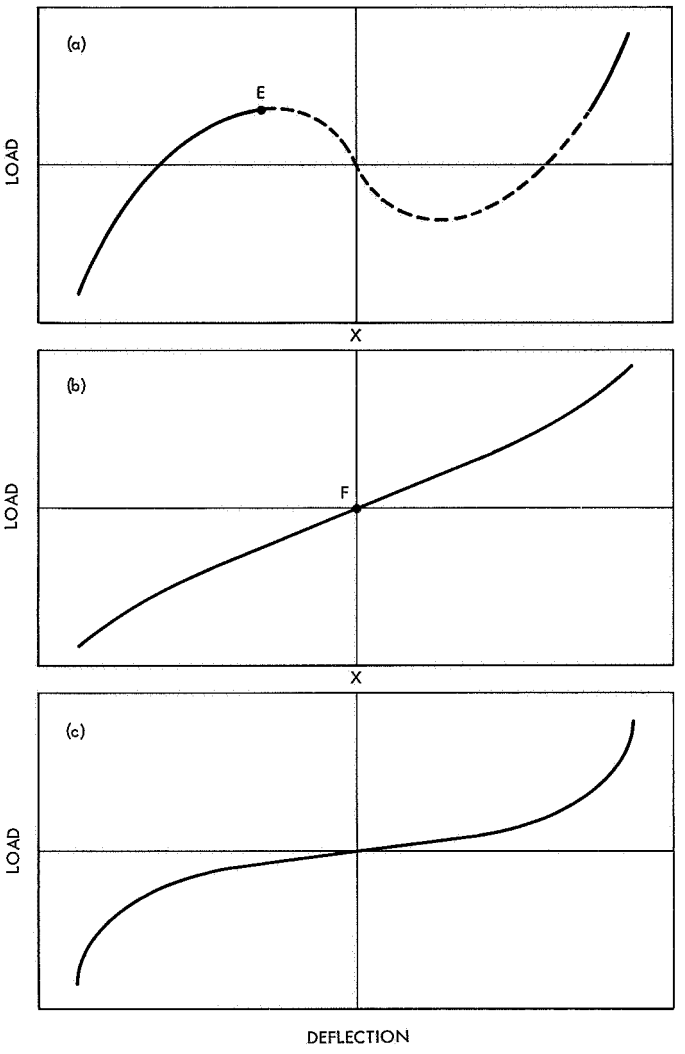

Fig. 42. Load deflection curves for springs in parallel

The dotted part of curve (a) was not observed because of measurement difficulties. It is hoped that later effort will confirm this speculation. Because the single spring curves (a) and (b) were not readily available, the springs were selected by measuring the load E for the unstable springs and the load F for the stable springs and mating springs for which the sum $E + F$ was that required. If the resulting curve (c) for each pair met the requirements for shape and load support, the spring pair was accepted.

The springs were mounted in a fixture which simulated the actual seismometer mounting. A load was slowly applied by means of a liquid system using linear differential transformers to provide load and position outputs (Fig. 43). The liquid system was chosen so as to provide a smooth continuous change of load with no additional

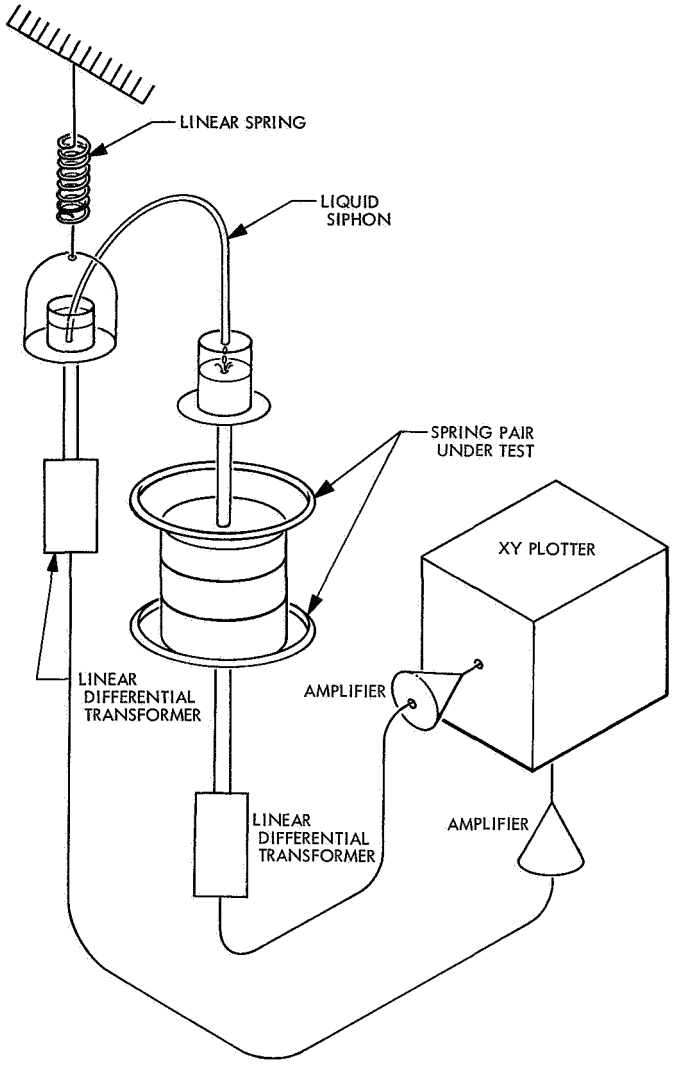

Fig. 43. Spring test arrangement

hysteresis. A linear spring, shown at the top of the figure, was used to transform the change of load to a change of position to which the linear transformer responded. The mass position was sensed by the other linear differential transformer, and these outputs were plotted automatically in real-time on an analog XY plotter. Since negative slopes (unstable) cannot be plotted by this arrangement, a further effort was planned to make the mass position the independent variable and read out the load so that continuous curves could be produced for unstable spring pairs.

It is difficult if not impossible to secure a valid spring curve directly for a single spring, but it is possible to get the single-spring curve by running three pairs of springs and constructing the single-spring curve by taking differences from the curves for each of the three pairs.

Another approach is to select three or more individual springs, including both stable and unstable samples, and secure composite curves for the three possible combinations of pairs. The only constraint must initially be that the resultant spring pair must exhibit stable performance for the test; that is, the resultant slope of the pair must always be positive. From the resulting three spring curves, sufficient data are available to establish mathematically the individual spring curves for each member, whether it be stable or unstable. As a next logical step, it should be a simple matter to digitize the data resulting from each spring test and develop a simple computer program to synthesize the spring curve resulting from any selected pair of springs. This approach should alleviate the difficulty encountered when a spring pair has an appreciable region of instability.

4. Thermal design. The temporal distribution of seismic disturbances cannot be predicted. Therefore, it is necessary and desirable to make seismic records over long periods of time. On the *Surveyor* mission, because of daylight operations on the spacecraft such as television scanning, it is unlikely that seismic disturbances would be detected during the day; hence it was necessary to plan for some lunar night operations of the seismograph. The lunar surface temperature range (+250°F in the day to −250°F at night) and the change from full solar input to lunar darkness provide a real challenge to the instrument designer. Seismometers designed for normal observatory applications exhibit temperature-induced drift, or variation in the rest position of the mass, which becomes increasingly apparent in longer-period instrument designs. This is due to the fact that long-period instruments require "softer" suspensions which yield large position changes for small force changes. In the case of short-period instruments such as the *Surveyor* design under discussion, stability problems over a normal range of temperature without thermal control would present no severe difficulty. However, the anticipated lunar temperature variation makes active thermal control necessary at least for the electronics.

As may be seen from Fig. 44, the sensor is enclosed within an outer thermal shell, which in turn is rigidly mounted to the spacecraft frame. The high thermal impedance from sensor to outer shell is a result of four factors:

(1) The lunar vacuum, or absence of atmosphere.

(2) Thermally insulating fiberglass cones supporting the sensor.

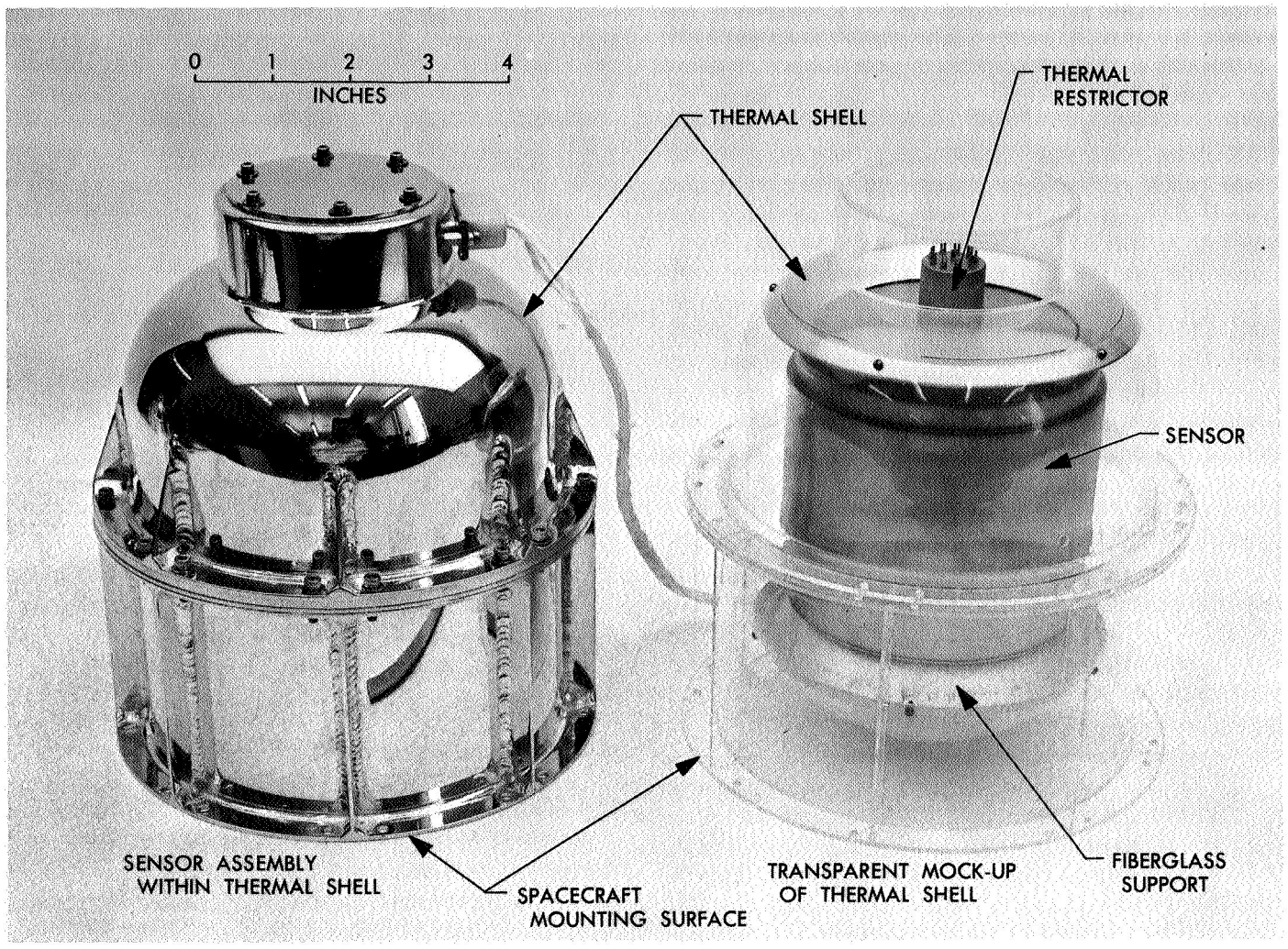

Fig. 44. Thermal shell and sensor support system

(3) Thermal radiation isolation blankets surrounding the sensor.

(4) Thermal restrictors within the electrical circuitry.

The fiberglass cones (Fig. 45) rigidly support the sensor assembly within the thermal housing, while minimizing the direct conduction of heat through the support. Composite cones were initially designed with balsa (grain parallel to cone element) to reduce the conductance and to absorb some of the shock loads. However, it was later found desirable to use the continuous fiberglass cone shown at the bottom of the figure rather than either the composite balsa cone or the fiberglass cone with thicker web and lightening holes. Rigid coupling of motion through the cones is essential to the normal function of the instrument; this requirement is fulfilled if the resonant

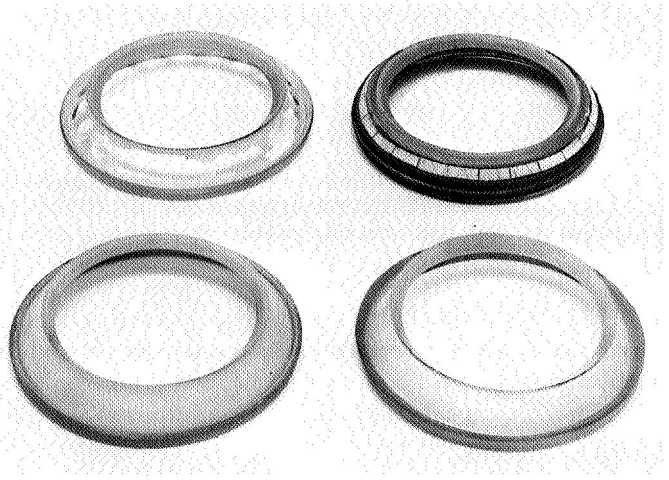

Fig. 45. Fiberglass support cones

frequency of the sensor-support system is well above the seismic spectrum of interest. The actual cones are sufficiently stiff so that no problem of poor seismic coupling was expected or detected.

Of more concern is the structural adequacy of the cones when subjected to shock and vibration during launch, flight, and landing modes. A tradeoff becomes evident, in that added thickness assures structural adequacy but at the expense of increased thermal conductance. The final instrument configuration uses cones with a fiberglass web of either 0.010- or 0.014-in. thickness. The 0.010-in. thickness has proven adequate for sensor support throughout a normal Type Approval test sequence; the web did fail catastrophically in the abnormal TA vibration test during which the specified excitation level was greatly exceeded.

The 0.014-in.-web cones were acquired as a possible substitute for the 0.010-in.-web cones in order to provide an additional margin of structural strength. While complete thermal tests on the 0.014-in. cones have not been made, preliminary estimates indicate that overall thermal isolation is not seriously compromised by the additional web thickness.

The thermal conduction losses which are introduced by the electrical connections are held to a minimum by insertion of the thermal restrictor. Each electrical circuit is completed through a short length of nichrome wire; in this way, considerable increase in thermal impedance is gained at the expense of negligible electrical resistance to the circuit involved.

The thermal blankets are used (within the housing) in order to minimize transfer of thermal energy by radiation. The necessity for these thermal blankets to minimize radiative heat losses was studied carefully in advance, and was the subject of three individual studies made on contract by General Electric, A. D. Little, and the Aeronutronic Division of Ford. After definite evidence of improvement using thermal blankets was established, the fabrication of flight hardware blankets was performed by General Electric.

JPL in-house thermal environmental testing has indicated that both the thermal blankets and the fiberglass support beams contribute to thermal isolation; the contribution of each is of a similar order of magnitude. The thermal test setup is shown in Fig. 46. The locations of the thermocouples are shown in Fig. 47; test results are given in Fig. 48.

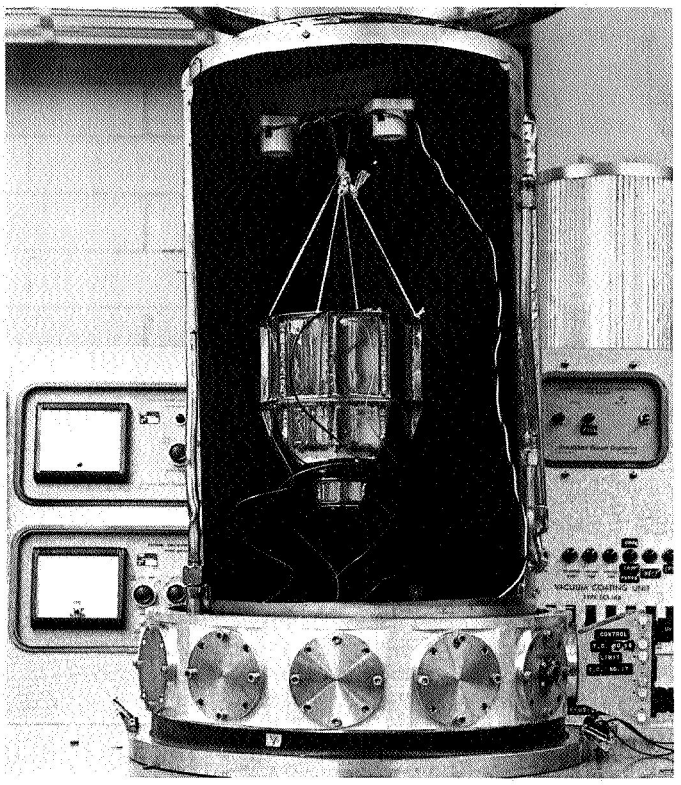

Fig. 46. Thermal–vacuum environmental test chamber

It is estimated that the heater, which has a rating of 1 W, will keep the seismometer at a temperature of 0°F throughout the lunar night with a 50% duty cycle. The heater will be switched on and off from earth as required. A desire by the experimenters to avoid having the heater switch on during a seismic signal led to the nonautomatic mode of thermal control.

The electronics, shown in Fig. 23, will be located in spacecraft compartment B, in which the temperature is controlled between −4 and 125°F.

F. Instrument Qualification

1. Seismograph testing and test results. Both the sensor and electronics associated with the *Surveyor* seismology experiment have been subjected to a more-or-less continuous sequence of tests from the inception of the instrument development program. The tests have been carried out to achieve a variety of objectives, viz., to establish preliminary design concepts for engineering evaluation, final design confirmation, acceptance of manufactured flight hardware, and Type Approval testing. Flight Acceptance tests will be performed prior to the flight of each instrument. In addition, certain testing activities have been performed which might properly be

described as "calibration"; these will be discussed in a subsequent section.

2. *Type Approval testing.* The TA tests were performed in two distinct and separate sequences, the electronics assembly and the sensor assembly each being tested individually. Certain test levels were different for each of the two test sequences owing to the different environment to which the sensor and the electronics would be subjected during flight and lunar operation.

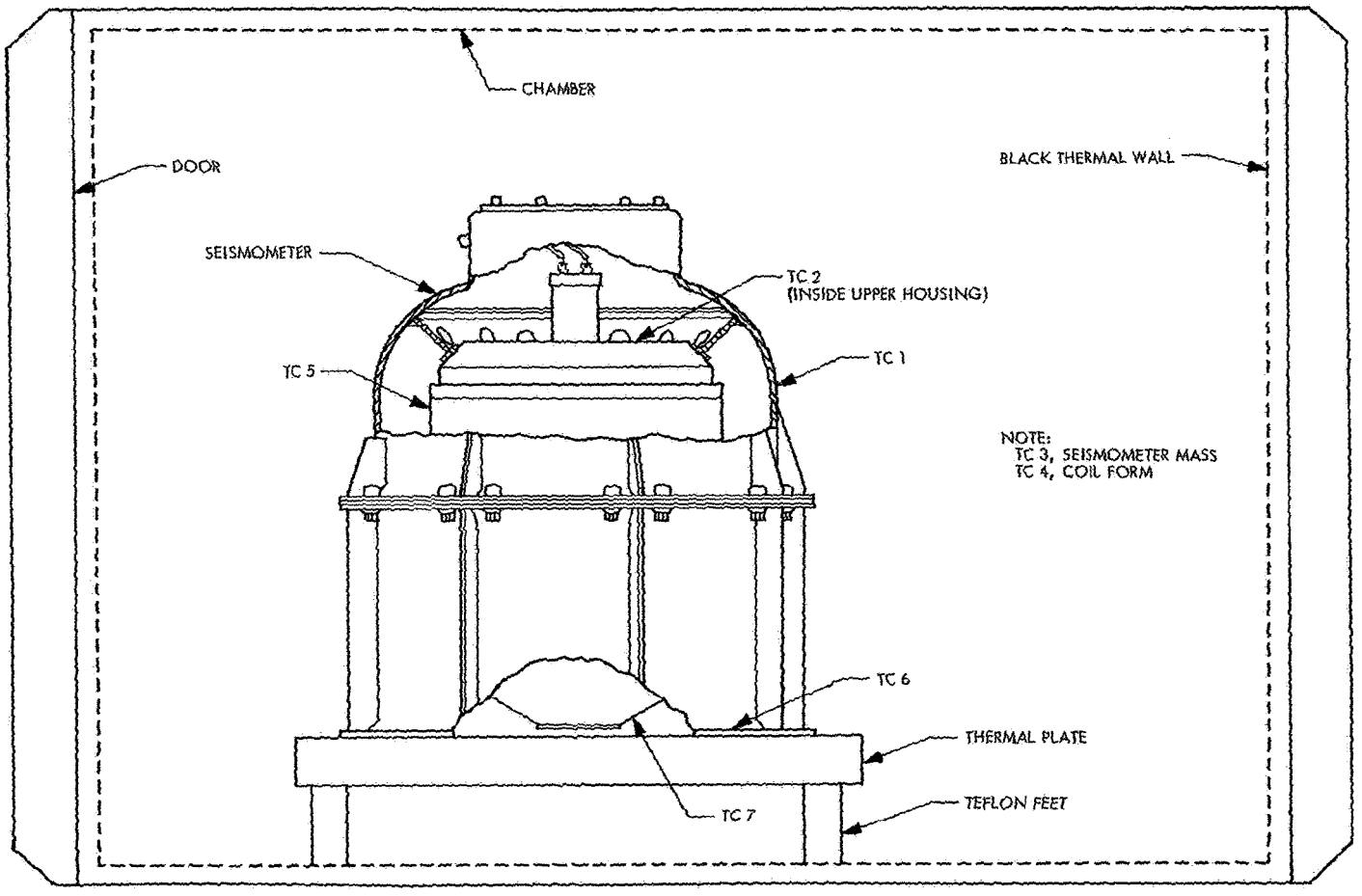

Fig. 47. Thermal–vacuum test configuration

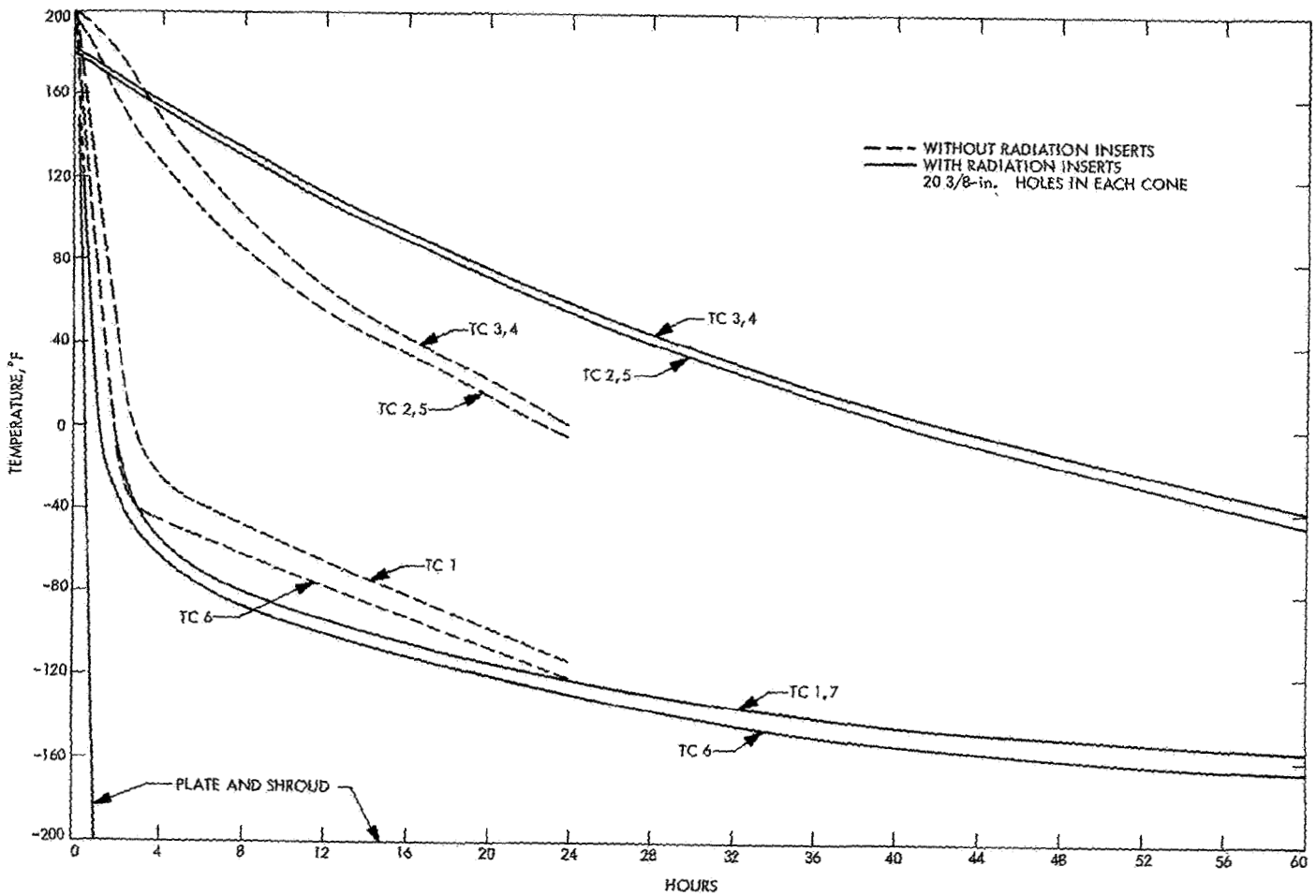

Fig. 48. *Surveyor* seismometer TCM 2 thermal vacuum test data

The test procedure requires that operational or functional checks be performed between the various TA environmental test items. In this way the integrity of the instrument was periodically reaffirmed, or, in the event of failure, the TA test step causing the failure would be immediately obvious.

In the case of the electronics assembly, no adverse effects were noticed at any time during or after TA testing. Accordingly, the electronics assembly has successfully passed the entire TA test except for the RF interference test step, which has yet to be performed. This step is most easily accomplished when the sensor is combined with the electronics assembly and simultaneous RF testing of both is done as one system.

Sensor unit P4A was subjected to a similar TA test sequence. Certain test steps (acceleration, shock, and acoustic tests) were routinely passed and require no further comment here.

Deviation was approved in the case of test step 7 (thermal–vacuum) in order to reduce the total time duration of the test to a reasonable value, while in no way altering the validity of the test. In lieu of "radiative control," the "heat exchanger" technique was used for thermal control in order to bring the sensor to its prescribed test temperatures more rapidly. In addition to the thermal plate as a heat sink (or source), layers of aluminum foil were added for conduction between the plate and the outer thermal shell of the seismometer. The effectiveness of the overall thermal design of the seismometer sensor is indicated by the fact that it took the better part of a week to arrive at the prescribed test temperatures within the vacuum chamber.

The sensor, unfortunately, did not pass the first TA test sequence because of two problems: (1) a catastrophic failure of the vibration exciter which subjected the instrument to shock excitation far in excess of its design limit, and (2) failure of the sensor mass caging mechanism (design deficiency) to restrain the mass against lateral vibration.

Each failure was analyzed and documented and adequate redesign measures were taken. The last TA test (except RF interference) proved the adequacy of the final sensor configuration. Owing to the nature of the seismometer, its signal, and its internal electronic circuitry, it is not expected that any difficulty will be encountered in the RF test.

The shock test was approached cautiously because of the sensor configuration. The mass of the assembled and caged sensor totals 2.66 kg, which must be supported by the web of the fiberglass support ring used to thermally insulate the sensor assembly from its outer thermal shell. The web, in various configurations, has been fabricated in thicknesses of both 0.010 and 0.014 in.

The adequacy of the 0.010-in. web was established by the TA testing, but the added safety factor provided by the 0.014-in. web seems worthwhile inasmuch as there is apparently no serious degradation of thermal insulation by the thicker material. The sensor, in fact, did survive the shock test with 0.010-in. webs in place; this test consisted of five 125-g pulses to each of three axes.

In the initial stages of the vibration test, difficulty was encountered when a malfunction in the vibration exciter system subjected the sensor to several moderately large vertical transients, followed by one final damaging shock. The source of the transients has been traced to a noisy connection in the patchcord system interconnecting the vibration source oscillator and the power amplifier which drives the shaker.

While the exact amplitude of the final transient is in doubt, we can set a lower threshold by considering that:

(1) The acceleration monitoring system was set for a normal recording range of up to 100 g.

(2) The linear range of the recording system extended to approximately 130 g.

(3) The saturation level of the recording system was approximately 160 g, and the record showed clear evidence of saturation levels of 160 g or more.

In an attempt to reconstruct the damaging shock level, the thermal control model sensor was fitted with a new set of 0.010-in. beams and subjected to axial shock excitation of gradually increasing intensity, terminating with approximately 250 g. While evidence of some folding in the fiberglass beam was observed, no complete structural failure was observed as was the case after the accidental excitation from the shake table. Thus, we estimate that the accidental loading must have been of the order of 250 g or more.

At this stage of testing the sensor was completely disassembled, inspected, and reassembled with 0.014-in. beams. After appropriate electrical calibration tests, the unit was again submitted for Type Approval vibration testing.

The complete vibration sequence was performed in accordance with the specification. As stated above, a second failure occurred which was documented in a Problem Failure Report. To summarize, the caging, or immobilizing scheme for the seismic mass, was found to be critically deficient. A design modification which was made to restrain the mass against rotation about the X and Y axes solved the problem.

Once again, the vibration test sequence was performed, and it was established that the sensor could withstand the vibration sequence. The sensor was then subjected to an acoustic test, which it passed successfully.

The thermal–vacuum test was essentially without incident except that the specified temperature extremes were considerably exceeded owing to a flaw in the temperature-sensing portion of the bench checkout equipment (BCE)[5] shown in Fig. 49. In spite of the excessive temperature extremes no damage was caused to the sensor. The squib circuit was fired, uncaging the seismic mass under vacuum conditions and at room temperature. The temporary deterioration of the vacuum soon disappeared and the cold cycle was initiated. Approximately five days were required to lower the sensor temperature to the indicated −101°C on the BCE meter. (Subsequent investigation has disclosed that the meter indicator was incorrect and the actual temperature was approximately −136°C.)

During the firing of the squib, current in the main coil was maintained at a value calculated to offset 5/6 g, thus simulating the gravity force which the lunar spring must overcome. The current was supplied from a power supply connected for constant-current output in order to present a near infinite (> 100 kΩ) impedance to the seismometer coil, thus eliminating damping effects due to the power supply. In addition, the normal amplifier load was synthesized by shunting an RC circuit across the main coil, 1600 Ω to represent the amplifier resistance, and 1000 mF in series to block the flow of dc current through this circuit from the constant-current power supply.

The seismic mass motion immediately following the squib firing was monitored by use of a Visicorder connected across the calibration coil. The resulting waveshape (Fig. 50) might be used for comparison with telemetered data from the lunar surface when the squib is fired. A similar waveshape would indicate normal mass release. However, it is unlikely that such a waveshape will be available via the telemetry link without severely overloading the amplifier. The turns ratio between calibration coil and main coil is 30:1, which means that the voltage output from the main coil will be approximately 30 times greater (or 29.5 dB) for the same amplitude of motion.

[5]Developed by Marshall Laboratories, Torrance, Calif.

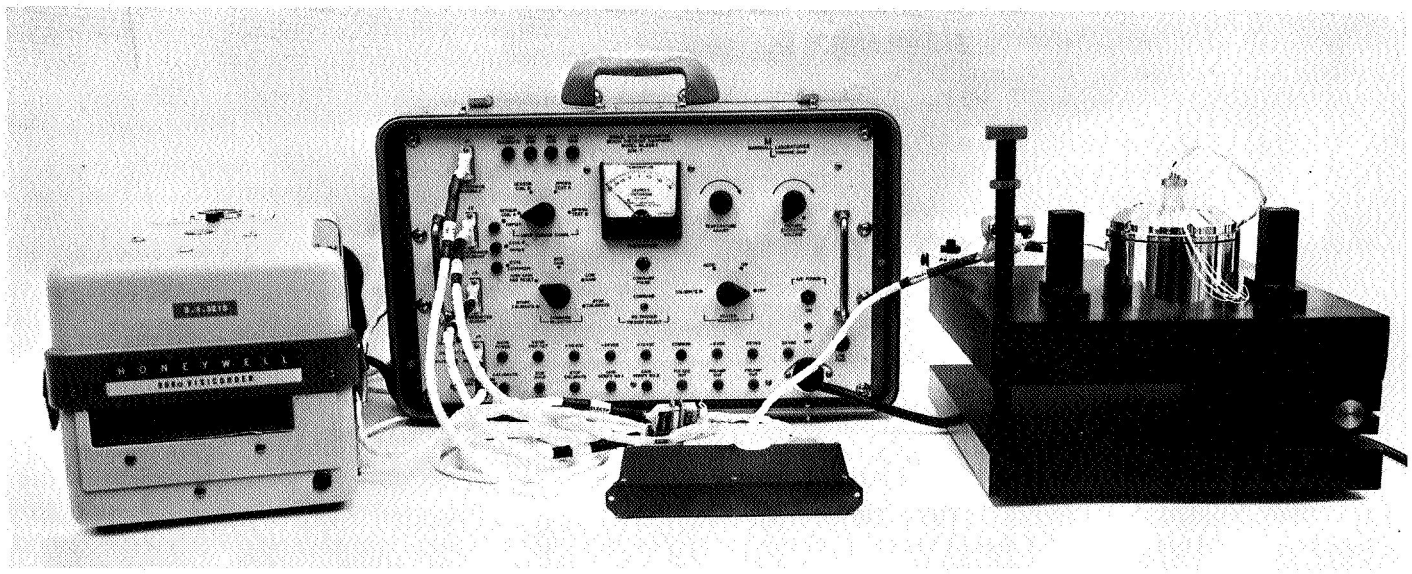

Fig. 49. Bench checkout equipment and calibration test fixture

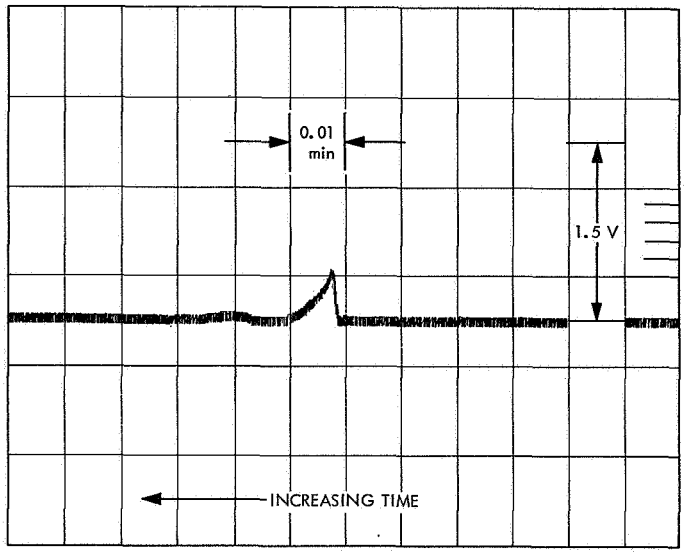

Fig. 50. Seismometer signal following squib firing

The connections to the calibration coil circuit were readily accessible during the thermal–vacuum test, but for lunar operation only the main coil will be available for output signal connection. Available amplifier gain levels are appropriate for the minute mass motions anticipated in normal seismic use, but the gross motion encountered at mass uncaging may generate a voltage in the main coil far in excess of the amplifier capability.

Primary temperature measurements of the sensor during the thermal–vacuum procedure were made by monitoring the Rosemount sensor which is mounted within the upper housing of the sensor. It was not possible to add an internal thermocouple, as the required additional circuit through the thermal restrictor was unavailable.

The bench checkout equipment was intended to operate in conjunction with the Rosemount sensor to give a visible temperature reading on the BCE panel. A 5-mA constant-current source is contained within the BCE circuitry, and the electrical meter face was rescaled to indicate sensor temperature directly. The temperature-vs-resistance curve for each Rosemount sensor was individually plotted and is included in the assembly documentation book for each sensor.

During the performance of thermal–vacuum tests, considerable discrepancy between BCE-indicated temperatures and other physical evidence became apparent. Subsequent investigations were performed to establish the source of error. Table 3 indicates the results.

Table 3. Bench checkout equipment calibration

Indicated temperature on BCE, °C	Actual temperature (from L and N thermocouple and potentiometer), °C	Temperature (from resistance reading referred to Rosemount curve), °C	Temperature (from thermometer within oven), °C
25	21	21	21.5
52	62.3	61	61.5
62.5	78.3	79	76
71	91	92	90
82	110.2	111	108.5

The correlation between the L and N thermocouple, Rosemount curve, and plain thermometer is obvious. Measurement of the constant-current source confirmed that it was properly adjusted to 5 mA. The only remaining conclusion is that the BCE meter scale and/or its associated circuitry have been improperly established. Although the accuracy checks were made only at room ambient temperature and higher, the linearity of the deviation clearly shows that negative BCE temperature readings were also in error.

On the basis of these tests, we may establish that the original thermal–vacuum test was conducted at temperatures ranging from −212 to +219°F, whereas the intended limits were −150 and +180°F. These results are also confirmed by the observed resistance values of the main and calibration coil windings and computation from the known thermal resistance coefficient of copper.

3. *Spring tests.* The pair of springs selected for test is assembled on a fixture (Fig. 43) which duplicates the mounting configuration of the seismometer. The springs are then loaded slowly, the resultant displacement of the spring-retaining frame being measured simultaneously. The two parameters (force and displacement) are sensed by differential transformers which generate the signals plotted on the XY recorder.

By appropriate calibration techniques (dc offset values and amplifier gain settings) the curve generated may be scaled to the engineering units on the preprinted spring-test form. A typical plot is shown in Fig. 39.

The natural period of the finished seismometer is related to the spring constant as follows:

$$T = 2\left(\frac{M}{K}\right)^{1/2}$$

where

T = natural period

M = suspended mass

K = spring constant

It is important to measure accurately the moving mass so that the natural period computed with the above formula will be accurate. The moving mass should include all pieces which are fully supported by the springs plus some fraction of the mass of each spring. The spring mass is sufficiently small so that we may estimate its effect without introducing significant error; in this case we include the mass of one entire spring and exclude the mass of the second spring as a satisfactory approximation.

Typical value for the moving mass of the *Surveyor* seismometer is 1680 g.

G. Calibration

Calibration of each of the sensors manufactured by Marshall Laboratories (including sensors P4A, P4B, and F-1 through F-4) was accomplished at the facilities of the Geotechnical Corporation, Garland, Texas. In addition, certain experimental results recorded during the Type Approval test sequence may be used to define sensor parameters not obtained during the Geotech calibration.

The Geotech calibration of sensor P4A is discussed below; similar calibrations of the other five sensors were performed and are included in unit history logs and/or seismometer assembly documentation.

In general, calibration of a seismograph instrument consists of establishing those instrumental parameters necessary to permit the seismologist to define completely the motion to which the instrument was subjected.

Instrumental parameters of primary interest to the seismologist include:

(1) Generator constant or sensitivity of the seismometer.

(2) Natural period or mechanical resonant frequency of the spring-mass system.

(3) Damping coefficient of the sensor.

(4) The amplitude and spectrum of the system input noise (presumably generated by the amplifier input stage).

Other significant information would include:

(1) The overload limitation of the system (presumably amplifier output) or the dynamic range of the system (system noise to overload ratio).

(2) The high-frequency response of the sensor (presumably limited by coil inductance as loaded by amplifier input resistance).

Unfortunately, these parameters are not constant, and it becomes necessary to determine the variations in the generator constant, natural period,and damping of the sensor as functions of both temperature and the position of the inertial mass. Variations in amplifier gain and input impedance should be known as functions of temperature and power supply voltage.

Certain parameters (e.g., generator constant and damping) are defined primarily for the main sensor coil but also have a meaning with respect to the calibration coil. These parameters are not all independent, and changes in period, damping, and generator constant, for instance, are interrelated.

Calibration of the sensors may be accomplished in several ways, each approach leading to the same end result. Each calibration method suffers from difficulties and inaccuracies, and this situation is further complicated by the fact that the calibration will be accomplished in the earth's gravity field, while ultimate instrumental application will take place in a lunar gravity field of approximately one-sixth that value. Theoretically, this is no problem, as it can be handled by computation leading to corrected values; but, in practice, certain measurements (e.g., those in which lunar springs are installed in the sensor) become more involved, and somewhat less accurate.

Probably the most straightforward calibration is by shake table excitation of the sensors to known levels and direct observation of the output voltage. This was done in the Geotech tests. The Geotech shake table, tiltable shake fixture, and seismometer are shown in Fig. 51.

In addition, certain measurements, taken in conjunction with the Type Approval testing sequence, will assist in computation of instrumental parameters. These values, while not of a precise nature, will tend to shed light on instrumental performance to be anticipated over environmental extremes.

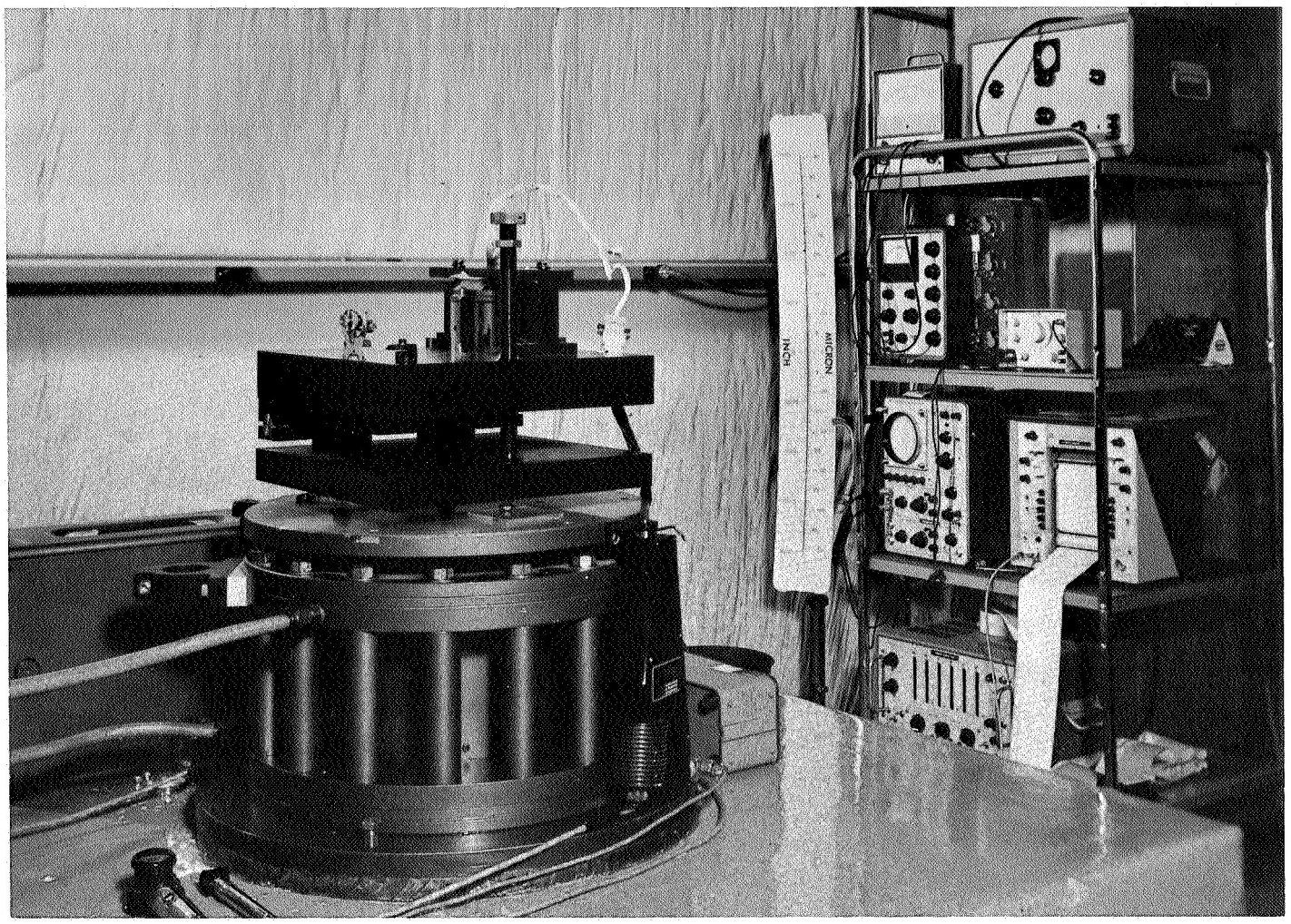

Fig. 51. Shake table and calibration instrumentation

The shake table results are documented in a series of curves furnished by Geotech. Several parameters were varied, including amplitude of shake table motion, frequency of excitation, magnitude of damping resistance, and tilt angle of sensor. All calibration data secured by Geotech were made with earth springs installed. Results are summarized in the Appendix.

In order to test (and calibrate) sensor performance with lunar springs installed it was necessary to supplement the load-bearing capability of the lunar springs to permit the seismic mass to float freely in its normal lunar position between the upper and lower limits of travel. It was essential that this additional support be supplied in such a manner that (1) it would not alter the instrumental damping characteristics during a dynamic test, and (2) it would not alter the shape of the spring characteristic curve. In addition, it was desirable that the technique be applicable to sensor testing under both vacuum and high- and low-temperature extremes and with the entire sensor housed in its thermal shell, i.e., in its final flight configuration. These last constraints (vacuum, temperature, flight configuration) effectively ruled out any possible mechanical or buoyancy schemes which might conceivably have been devised to temporarily offset five-sixths of the earth's gravity force.

The scheme which was adopted, and which proved quite satisfactory, involved the application of direct current into the main sensor coil, with an upward force thus being generated by interaction with the sensor's magnetic flux. There are, however, many obscure pitfalls to be avoided in using this technique!

The circuitry required to implement this scheme (Fig. 52) required three series-connected Kepco power

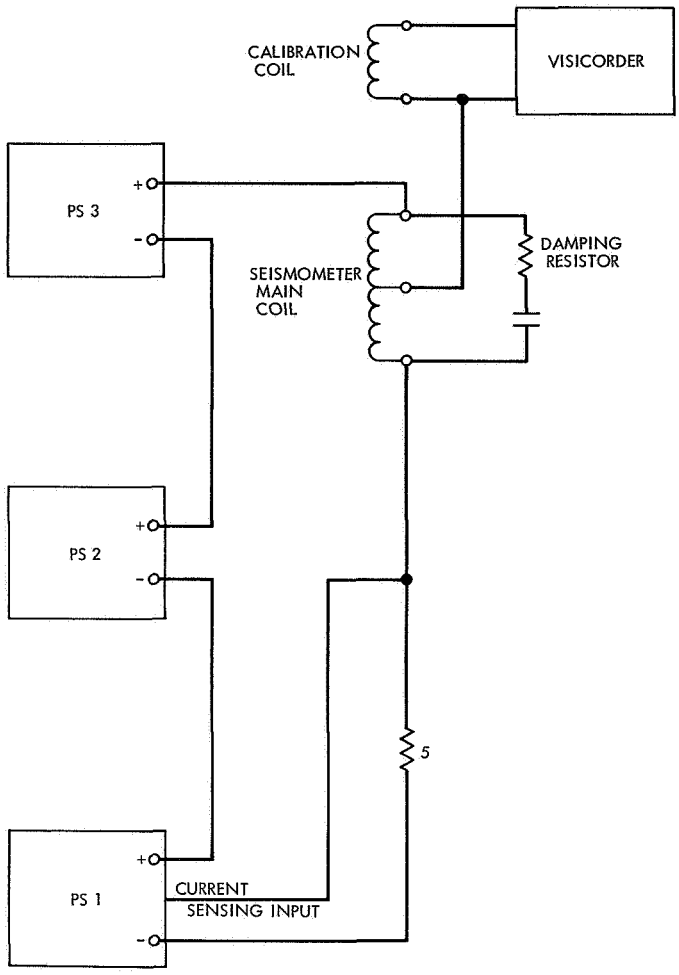

Fig. 52. Electrical force generation

supplies. Power supply 1 was constant-current-connected while power supply 2 and power supply 3 retained their normal constant-voltage configuration.

The constant-current supply effectively presents a high impedance to the seismometer coil so as to minimize the damping effect to the seismometer when motion occurs. The additional two power supplies merely provide sufficient voltage to drive the necessary current through the resistance of the main coil.

In practice, satisfactory, if not ideal, results were obtained with an effective power supply impedance of 100 kΩ. With minor circuit modifications to the power supply amplifier, this constant-current operation was extended to reasonably high frequencies. Obviously, this frequency bound had to be well beyond frequencies of interest in the seismic region. In addition, some effort was required to assure complete power supply stability and freedom from oscillation throughout the frequency spectrum of interest.

In practice, these requirements were met adequately, and the power supply support technique worked well. For damping purposes, an external resistance may be shunted across the main coil simultaneously, provided that either (1) dc current flow is blocked by a suitably large capacitor, or (2) the power supply and resistor wattage ratings are both sufficiently large to handle the additional dc power flow. If a blocking capacitor is used, low-frequency phase shift within the spectrum of interest must be considered, particularly as it alters the damping characteristics of the seismometer near its natural period.

The output from the seismometer coil may be monitored by the Visicorder, as in conventional calibration, by connection across either the main coil or the calibration coil. If connected to the main coil, once again a suitable blocking capacitor is required to prevent dc current flow into the Visicorder, and low-frequency phase shifts should not be overlooked.

As an attractive alternate, direct connection of the Visicorder to the calibration coil permits isolation from the constant-current dc source, provided adequate signal is generated in the calibration coil for recording purposes. The signal voltage generated in either the main coil or calibration coil is linearly related by a constant proportionality, so either coil is useful for output purposes. When damping must be considered, the total system damping may be applied to either coil or distributed between coils as desired.

The interaction of direct current in the main coil of the seismometer with the magnetic flux in the gap results in a force which acts upon the inertial mass. For static equilibrium (disregarding the unavoidable small motion introduced by seismic background) the resultant of all forces acting on the mass must be zero. These forces are:

(1) Gravity force MG.

(2) Spring force KX.

(3) Electrical force BLI.

(The engineering symbols carry their customary connotation.)

By injection of direct current into the main coil in varying amounts it is possible to move the mass to any position between its two limit stops; a plot of mass position vs direct current is valuable in analysis of the sensor performance.

The stop-to-stop motion of the mass is approximately 0.75 in. in the *Surveyor* seismometer, and near each end of the travel there is an appreciable variation in flux density in the magnetic gap which is responsible for variation in both generator constant and damping as a function of mass position.

When injecting direct current into the main coil, the force-generated *BLI* will vary with mass position due to the nonuniform flux-density distribution. While this nonuniformity can be evaluated directly by use of a fluxmeter probe within the gap, it is difficult to obtain sufficient accuracy and repeatability for calibration purposes.

An alternate indirect method is to plot mass position vs direct current injected into the main coil with the seismometer first in an upright and then in an inverted position. The apparent "reversal" of gravity with respect to a coordinate system centered on the seismometer permits separation of the forces into individual gravity, electrical, and mechanical spring components.

Figure 53 is a plot of "upright" and "inverted" forces for sensor P4A. These values were taken with nonpreformed spring blanks (Elinvar-Extra 1245 and 1445) installed. The third curve (shown dashed) represents the current required to offset the total gravity force only and is derived by averaging the "upright" and "inverted" current values for each displacement. The concave upward shape of this "gravity only" curve indicates that more current is required to offset a constant gravity force near the top and bottom limits of mass travel because of reduced magnetic flux intensity at these locations.

The degree of flux deterioration as a function of mass position is plotted in Fig. 54. For reference purposes, it is assumed that the maximum flux position (i.e., minimum current position) represents 100% "efficiency," and the percent deterioration is referred to that central value. As indicated, flux variations of 7.5 to 8% are encountered near the limits of mass travel. It should be noted that these values are averaged over the length of the coil winding; integration is automatically accomplished by the coil in the measurement process, producing a distinct advantage over the fluxmeter and manual-averaging method.

As a measure of instrumental deterioration resulting from Type Approval testing, electrical force measurements were made before and after the vibration and the thermal–vacuum test steps. The results are plotted in Fig. 55. In this instance the reversed gravity (inverted sensor) position was unnecessary; comparison of before and after readings was all that was required. The three curves plotted represent:

(1) Before vibration test.

(2) After vibration but before thermal–vacuum test.

(3) After thermal–vacuum test.

These data were secured with lunar (preformed) springs installed within the sensor. We can conclude that:

(1) The vibration test resulted in slight departure from the preceding condition. It is debatable whether the

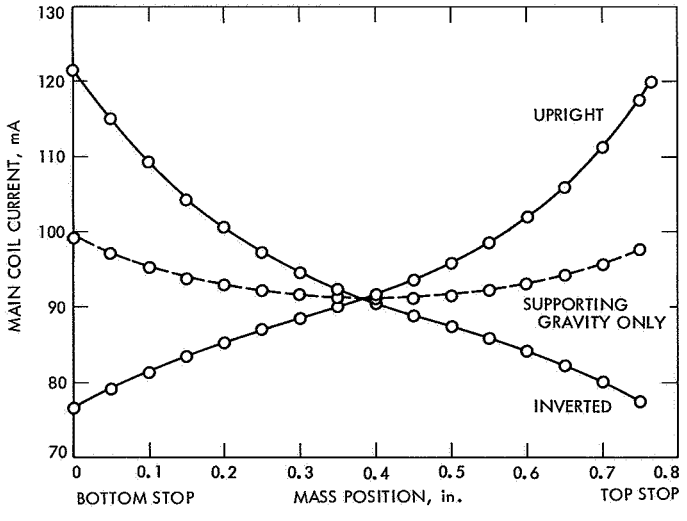

Fig. 53. Coil current vs spring deflection for nonpreformed springs

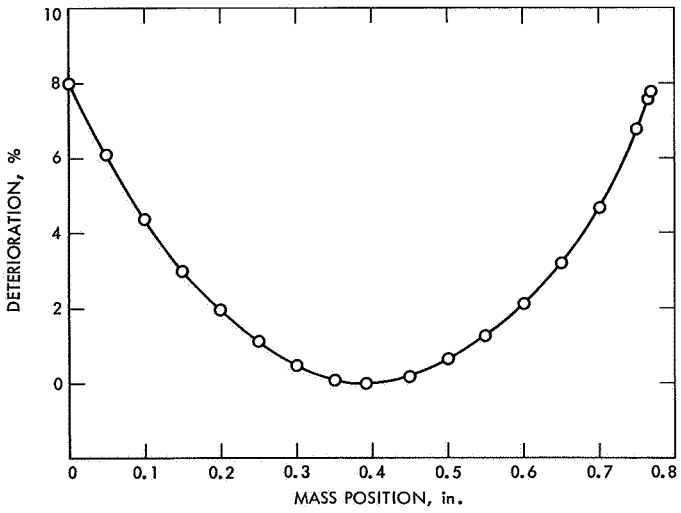

Fig. 54. Deterioration of magnetic field vs position

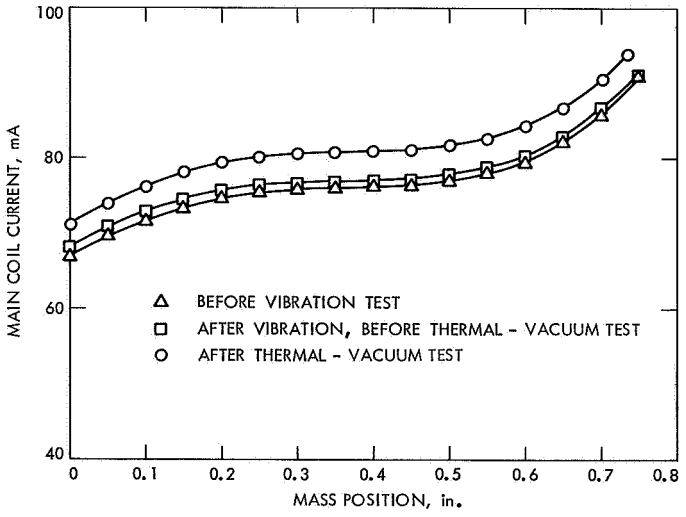

Fig. 55. Coil current vs mass position as a function of vibration and thermal vacuum

additional electrical force required results from a reduction in magnetic flux intensity or a reduction in preload capacity of the lunar springs.

(2) The thermal–vacuum test resulted in a larger degree of deterioration. Again, it is unknown whether the cause is flux change or mechanical spring changes.

While the individual changes in current reading (in percent) are slight, analysis of the deviations and least-squares fit of the difference between individual curves indicates that the deviations are real and of significant amplitude.

In the use of electrical force to support a portion of the mass, an unstable condition is frequently encountered, particularly with lunar springs, which give an extremely long period. This instability is a result of the mass seeking a stable position in which the positive slope of the "spring curve" is greater than the negative slope of the "spring curve" of the "synthetic" spring which appears because of electrical force variations induced by flux variations.

For calibration purposes, it is strongly recommended that further data be taken over temperature ranges similar to those used for Type Approval testing. By eliminating the vacuum requirement, more accurate and complete data could be secured.

References

1. MacDonald, G. J. F., "Interior of the Moon," *Science,* Vol. 133, pp. 1045–1050, April 1961.
2. Press, F. P., Buwalda, P. W., and Neugebauer, M., "A Lunar Seismic Experiment," *J. Geophys. Res.,* Vol. 65, pp. 3097–3105, October 1960.
3. Bolt, B. A., "Spheroidal Oscillations of the Moon," *Nature,* Vol. 188, p. 1176, December 1960.
4. Bolt, B. A., "Theoretical Phase Velocities for a Lunar Seismic Experiment," *J. Geophys. Res.,* Vol. 66, pp. 3513–3518, October 1961.
5. Carr, R., and Kovach, R. L., "Toroidal Oscillations of the Moon," *Icarus,* Vol. 1, pp. 75–76, 1962.
6. Sutton, G. H., Neidell, N. S., and Kovach, R. L., "Theoretical Tides on a Rigid Spherical Moon," *J. Geophys. Res.,* Vol. 68, pp. 4261–4268, July 1963.
7. Harrison, J. C., "An Analysis of the Lunar Tides," *J. Geophys. Res.,* Vol. 68, pp. 4269–4280, July 1963.

References (contd)

8. Lehner, F. E., Witt, E. O., Miller, W. F., and Gurney, R. D., "A Seismometer for Lunar Experiments," *J. Geophys. Res.*, Vol. 67, pp. 4779–4786, November 1962.

9. *Design and Construction of a Lunar Seismograph Prototype Model,* Final Report, Contract JPL 950157, submitted to Jet Propulsion Laboratory by Lamont Geological Observatory, Columbia University, New York, 1962.

10. Sutton, G. H., and Latham, G., "Analysis of a Feedback Controlled Seismometer," *J. Geophys. Res.*, Vol. 69, pp. 3865–3882, September 1964.

11. Thanos, S. N., "A Low-Noise Transistorized Seismic Amplifier," *Bull. Seismological Soc. Am.*, Vol. 54, pp. 347–368, February 1964.

12. Dewitt, D., and Rossoff, A. L., *Transistor Electronics,* McGraw-Hill Book Company, Inc., New York, N.Y., 1957, pp. 219–222.

Appendix

Vibration Data for *Surveyor* Single-Axis Seismometer P4A

Figures A-1, A-2, and A-3 present seismometer P4A calibration data.

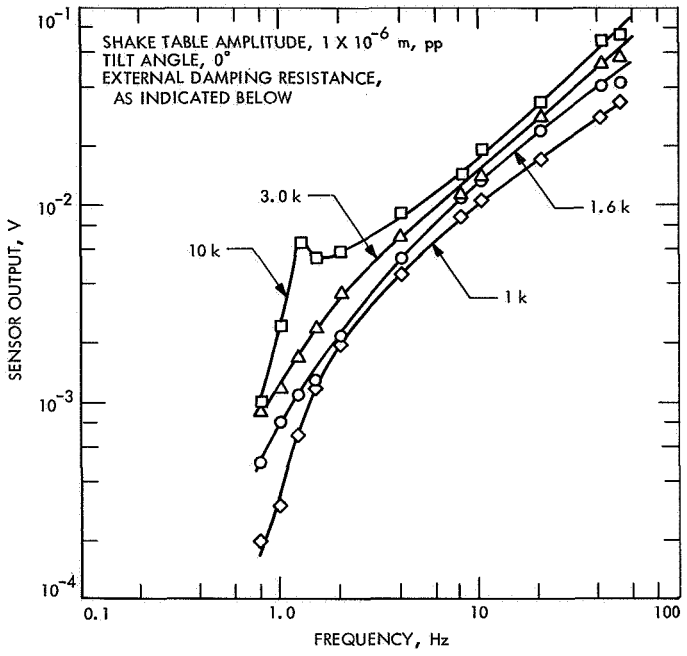

Fig. A-1. Seismometer P4A calibration data, damping resistance

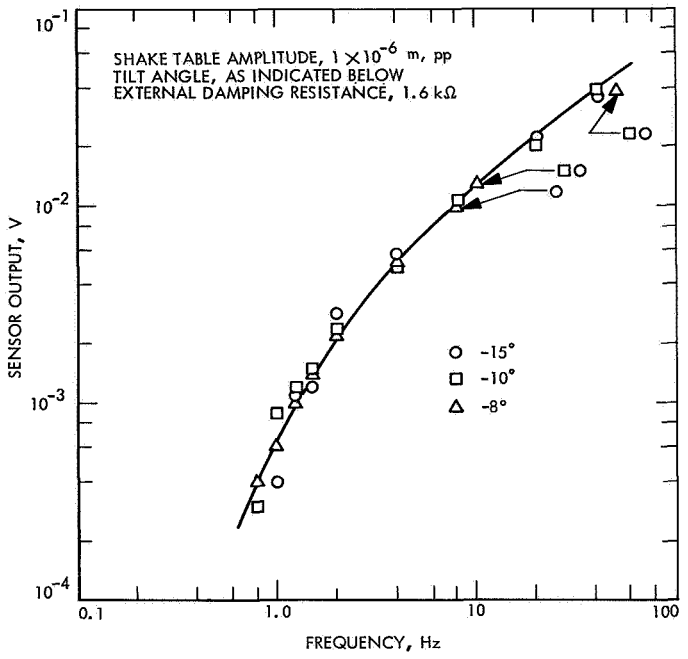

Fig. A-2. Seismometer P4A calibration data, tilt angle

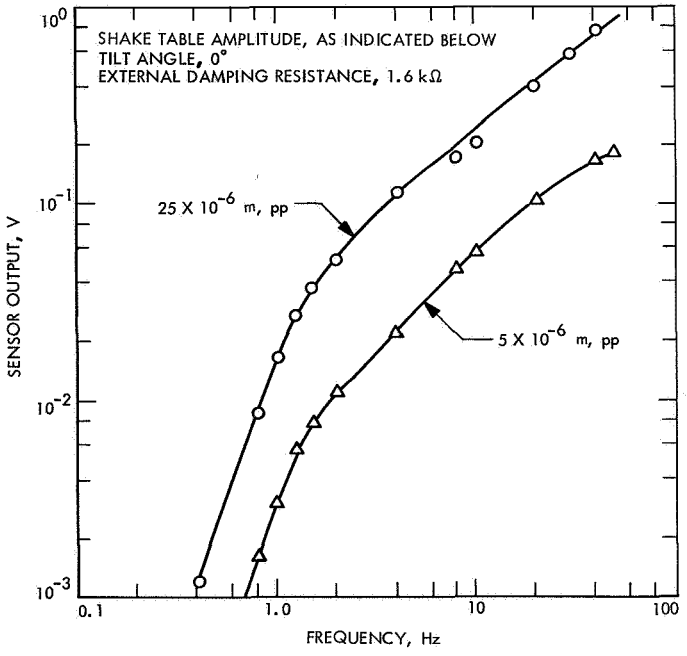

Fig. A-3. Seismometer P4A calibration data, shake table amplitude